Teotia, Arun; Dienel, Kasper; Qayoom, Irfan; van Bochove, Bas; Gupta, Sneha; Partanen, Jouni; Seppälä, Jukka; Kumar, Ashok

Improved Bone Regeneration in Rabbit Bone Defects Using 3D Printed Composite Scaffolds Functionalized with Osteoinductive Factors

Published in:
ACS Applied Materials and Interfaces

DOI:
10.1021/acsami.0c13851

Published: 28/10/2020

Document Version
Peer-reviewed accepted author manuscript, also known as Final accepted manuscript or Post-print

Please cite the original version:
Teotia, A., Dienel, K., Qayoom, I., van Bochove, B., Gupta, S., Partanen, J., Seppälä, J., & Kumar, A. (2020). Improved Bone Regeneration in Rabbit Bone Defects Using 3D Printed Composite Scaffolds Functionalized with Osteoinductive Factors. *ACS Applied Materials and Interfaces*, *12*(43), 48340-48356. https://doi.org/10.1021/acsami.0c13851

Improved bone regeneration in rabbit bone defects using 3D printed composite scaffolds functionalized with osteoinductive factors

Arun Kumar Teotia[1], Kasper Dienel[2], Irfan Qayoom[1], Bas van Bochove[2], Sneha Gupta[1], Jouni Partanen[3], Jukka Seppälä[2], Ashok Kumar[1,2,*]

[1]Department of Biological Sciences and Bioengineering, Indian Institute of Technology Kanpur, Kanpur-208016, India

[2]Polymer Technology, School of Chemical Engineering, Aalto University, Espoo-02150, Finland

[3]Department of Mechanical Engineering, Aalto University, Espoo-02150, Finland

***Corresponding Author:**

Prof. Ashok Kumar

Department of Biological Sciences and Bioengineering,

Indian Institute of Technology Kanpur (IITK), Kanpur, UP-208016, India

Email: ashokkum@iitk.ac.in

Phone: +91-512-2594051

Abstract

Large critical size bone defects are complicated to treat and in many cases autografts become a challenge due to size and availability. In such situations, a synthetic bone implant that can be patient specifically designed and fabricated with control over parameters such as: porosity, rigidity and osteogenic cues, can act as a potential synthetic bone substitute. In this study we produced photocuring composite resins with poly(trimethylene carbonate) containing high ratios of bioactive ceramics and printed porous 3D composite scaffolds to be used as bone grafts. To enhance the overall surface area available for cell infiltration the scaffolds were also filled with a macroporous cryogel. Furthermore, the scaffolds were functionalized with osteoactive factors: bone morphogenetic protein (BMP) and zoledronic acid (ZA). The scaffolds were evaluated *in vitro* for biocompatibility and for functionality *in vivo* in critical bone defects (~8 mm) in two clinically relevant rabbit models. These studies included a smaller study in rabbit tibia and a larger study in the rabbit cranium. It was observed that the bioactive molecule functionalized 3D printed porous composite scaffolds provide an excellent conductive surface inducing higher bone formation and improved defect healing in both critical size long bone and cranial defects. Our findings provide strong evidence in favour of these composites as next generation synthetic bone substitutes.

Keywords: stereolithography, polymer composite, bone regeneration, poly(trimethylene carbonate), additive manufacturing, bioactive, rabbit

1. Introduction

Cranioplasty, tumor resections, congenital disorders and accidents can lead to both orthopedic and maxillofacial bone defects [1–3]. Bones have an inherent capacity of regeneration, restoring both structural and cellular composition of damaged tissue through a cascade of orchestrated anabolic and catabolic activities [4,5]. The complex healing process involves activation of several signaling pathways (Wnts, bone morphogenetic proteins (BMPs) and fibroblast growth factors (FGFs)) [6–9] having a high gene expression overlap with that of embryonic bone development [10,11]. The healing of defects usually happens without major intervention if the defect is smaller than 2-2.5 times the diameter of the affected bone. Defects larger than that fail to heal spontaneously and are considered critical sized defects [12]. For example, in humans a defect of 2.5 cm in tibia is considered critical while the limit is much higher (>6 cm) for defects of the femur [13,14]. For cranioplasty, a defect >25 cm^2 is considered challenging [1,15].

Although autografts are considered the gold standard, secondary surgery and size limitations restrict the reconstructions of for large sized bone defects [16,17]. Moreover, other options such as allografts and xenografts have issues with infection, graft integration/rejection and early resorption. It is further observed that extensive resorption of calcium salts and morselized or cancellous bone grafts implanted in defects larger than 6 cm fail to result in healing [18,19], especially in cranioplasty [15–17]. These unsatisfactory outcomes necessitated to investigate metallic and polymeric alternatives capable of providing support and stability during the healing of defects. However, interference during imaging, inflammation of surrounding tissue from corroding materials [20], stress [21] and thermal necrosis [22] pose constraints with the materials explored. Ceramic bone substitutes (zirconium, tricalcium phosphate (TCP) and hydroxyapatite (HA)), have overcome some of those limitations [23]. Although ceramics are highly biocompatible and osteoconductive [24,25] their brittle nature hampers formability, limiting their use to fillers for small defects with simple geometries [26]. To overcome the brittle nature of ceramics researchers have explored their composites with several polymeric materials such as poly(methyl methacrylate) (PMMA) [27], poly(lactic acid) (PLA) [28], poly(lactic-co-glycolic) acid (PLGA) [29], poly(caprolactone) (PCL) [30], poly(trimethylene carbonate) (PTMC) [31], chitosan, collagen, and gelatin [32,33].

Polymer-composites also enable controlled local release of loaded osteoinductive factors (BMPs, bisphosphonates, platelet-derived growth factor (PDGF) and zoledronic acid (ZA)). Local delivery of bioactives have been found effective in enhancing bone formation and integration of implants at doses lower than clinically given systemic doses. This low dose delivery also eliminates dose dependent side effect issues [34–36]. The presence of such osteoactive molecules enables enhanced cell infiltration/differentiation and bone formation. We have previously developed macroporous composite cryogel scaffolds providing enhanced surface area with interconnected porous network for cell infiltration [32,33,35]. These cryogels provided effective release of the loaded bioactive molecules (BMP and ZA) in a sustained manner.

With diverse size and anatomical geometries, engineering a bone graft for defect filling poses additional challenges. Here additive manufacturing (AM) can provide feasible solutions. Stereolithography (SLA) is an AM method based on the layer-by-layer solidification of a photo-crosslinkable resin. It enables fabrication of designed constructs with precise control over resolution, complex pore geometries, and interconnectivity [37] which play a crucial role in overall scaffold strength and cell infiltration [38,39]. As such, SLA provides ease of fabrication of patient specific structures matching the defect geometry and dimensions [15,31]. Additionally, resins containing osteoconductive ceramics can be used to prepare bone implants [28], with reasonably high ceramic concentrations.

PTMC is a biodegradable aliphatic polycarbonate with excellent biocompatibility [40], no harmful degradation products [41] and slow surface erosion based degradation [42,43]. It has low elastic modulus and tensile strength and lacks form-stability [44]. Form-stable networks with improved modulus and tensile strength can be prepared by crosslinking. These networks can be prepared from high molecular weight PTMC by gamma irradiation [45] or from methacrylate end group functionalized low molecular weight PTMC by photo-crosslinking [46]. The mechanical properties of photo-crosslinked PTMC networks can be tailored by altering the polymer molecular weight [46]. To further reinforce the polymer, composites can be prepared with the matrix allowing incorporation of substantial amounts of TCP or HA improving the

stiffness and toughness of the materials considerably [31,47]. The application of photo-crosslinkable PTMC in SLA has been extensively studied [37,48]. In studies targeting for bone implants [47,49,50], SLA fabricated composite scaffolds including high amounts of ceramics have demonstrated direct availability of ceramics on the surface of the scaffolds, a feature unique to SLA fabricated scaffolds. The direct availability of the osteoconductive ceramics on the surface also enhances bone formation [50].

While previous studies with SLA fabricated scaffolds containing HA or TCP showed enhanced bone formation, the materials in these studies did not contain any osteoinductive factors such as BMP or ZA [49,50]. Other studies showed that including BMP and ZA in cryogel scaffolds had a positive effect on bone formation [32,35], but scaffolds prepared from these materials lack the mechanical strength of SLA fabricated PTMC composite scaffolds [33,47], particularly when considering larger size bone defects. Our hypothesis for this study was that by preparing PTMC scaffolds containing either HA or TCP using SLA and subsequent functionalization of these scaffolds with BMP and ZA we would obtain scaffolds with good mechanical properties and improved bone formation as compared to these types of structures separately. In addition, we aimed to increase the surface area available for bone growth by infiltrating the SLA prepared scaffolds with macroporous composite cryogels prepared *in situ*. The performance of the obtained structures was evaluated *in vitro* as well as *in vivo* in two separate critical size bone defect models in rabbits.

2. Materials and Methods

2.1 Materials

1,3-trimethylene carbonate (TMC) (Forusorb) was purchased from Huizhou Foryou Medical Devices (China) and used without any further purification. Stannous octoate ($Sn(Oct)_2$), Dulbecco's modified Eagle's medium (DMEM), β-tricalcium phosphate (TCP), 3-(4,5-dimethylthiazol-2-yl)-2,5-diphenyl tetrazolium bromide (MTT), 4′,6-diamidino-2-phenylindole (DAPI), phalloidin-fluorescein isothiocyanate (FITC), gelatin and glutaraldehyde were purchased from Sigma (USA). 1,1,1-tris(hydroxymethyl) propane, hydroquinone, methacrylic anhydride, trimethylamine, diphenyl(2,4,6-trimethylbenzoyl)phosphine oxide (TPO-L), Orasol Orange-G, dichloromethane, ethanol, propylene carbonate, deuterated chloroform ($CDCl_3$) and sodium borohydride were purchased from Merck (Germany). Recombinant human bone morphogenetic protein-2 (BMP) was purchased from Medtronics (USA), zoledronic acid (ZA) (Zoldonat) was purchased from Natco Pharma Ltd (India) and fetal bovine serum (FBS) was purchased from Gibco (USA). Penicillin-streptomycin antibiotic cocktail was purchased from Hi-Media (India), isoflurane (Forane) from Abbott (India), Ceftriaxone (Cefaxone) from Lupin (India), Tramadol (Dolphan) from GreenCross Remedies (India) and povidine-iodine (Betadine) from Win-Medicare (India). Nano-hydroxyapatite (HA) used was synthesized in the laboratory using the protocol as described elsewhere [51].

2.2 Synthesis and characterization of poly(trimethylene carbonate) macromer

Poly(trimethylene carbonate) (PTMC) was synthesized by ring-opening polymerization of 1,3-trimethylene carbonate, using 1,1,1-tris(hydroxymethyl) propane (0.01 mol/mol TMC) as initiator to obtain a three-armed oligomer. The reaction was catalyzed by $Sn(Oct)_2$ (0.0002 mol/mol TMC) and carried out at 130 ºC for 48 hours under N_2 atmosphere. The reaction was followed with ^1H nuclear magnetic resonance (NMR) spectroscopy (Bruker AVANCE III 400 MHz), based on which also the monomer conversion and number-average molecular weight were analyzed. For NMR, samples were dissolved in deuterated chloroform. The hydroxyl terminated oligomer was functionalized by dissolving it in dichloromethane (1.3 ml/g oligomer) and adding methacrylic anhydride (6.0 mol/mol oligomer) in

the presence of hydroquinone (0.1 wt%) and triethylamine (6.0 mol/mol oligomer). The degree of functionalization of the methacrylated PTMC oligomer (macromer, PTMC-tMA) was calculated from NMR analysis. After functionalization at room temperature for 4 days the solution was precipitated in cold ethanol and dried in vacuum at 40 ºC until a constant weight was obtained.

2.3 Preparation of scaffolds

Three photocrosslinkable resins were prepared for stereolithography (SLA) based additive manufacturing: a neat PTMC resin and two composite resins with a polymer/ceramic ratio of 60:40 (w/w). The polymer was dissolved in propylene carbonate at approximately 70°C in order to achieve a resin with a viscosity that can be used in stereolithography. Following addition of the solvent, TCP or HA were mixed into the composite resins to generate polymer-ceramic composite resins. Diphenyl(2,4,6-trimethylbenzoyl)phosphine oxide (TPO-L) was used as photoinitiator and Orasol Orange dye was added to control the light penetration depth into the resin. The final resin compositions where as follows: PTMC neat resin (51.5 wt% PTMC, 44.9 wt% PC, 3.5 wt% TPO-L, 0.03 wt% dye) and PTMC composite resins (27.7 wt% PTMC, 18.4 wt% β-TCP/HA, 52.5 wt% PC, 1.4 wt% TPO-L, 0.01 wt% dye).

Using Mathmod 8.0 (https://sourceforge.net/projects/mathmod/), CAD-files of cylindrical scaffolds with 3D gyroid pore architecture were generated using trigonometric functions described previously[52]. To obtain scaffold with dimensions of 10 mm × 5 mm (diameter × height) and a 720 µm pore size, 500 µm wall thickness and ~76% porosity Rhinoceros 4 (Robert McNeel and Associates) was used. The scaffolds were manufactured using a digital light processing (DLP) SLA device (Envisiontec Perfactory III Mini SXGA+, Germany). The building was performed as previously described [47]. Briefly, by scaling the designs prior to printing, isotropic shrinkage during solvent extraction was taken into account. During printing, each layer was exposed to light for 12 s at an intensity of 700 mW/dm^2 with a wavelength of 400-550 nm. The resin was optimized to print at a layer thickness of 50 µm by making a working curve to determine the optimal amount of dye. Post-fabrication, propylene carbonate was extracted from the swollen scaffolds through a solvent exchange with ethanol. The extraction was started with a propylene carbonate

(PC)/ethanol (60:40 v/v) mixture, following changing of the extraction mixture daily while lowering the amount of ethanol by 10 vol% until extracting with only ethanol. Finally, samples were dried at 40 °C in vacuum until constant weight.

To generate cryogel infiltrated 3D PTMC + HA or TCP scaffolds, the empty porous space of selected scaffolds was further infiltrated with macroporous composite cryogels [53–55]. Briefly, composite blends of gelatin-HA and gelatin-TCP (60:40% w/w) were prepared by dissolving appropriate amounts of gelatin in deionized H_2O and dispersing the ceramic component in polymer solution. The composite blends were homogenized thoroughly for uniform distribution of inorganic components, followed by cooling of the blends by keeping at 4 °C. To the precooled blends, aqueous solution of glutaraldehyde (0.2% w/v) was added and mixed thoroughly. The composite blend was impregnated into porous cavities of the scaffolds with constant vibration for uniform infiltration, following which the scaffolds were immediately transferred to -15 °C for 12 hours inducing macroporous composite cryogel formation. Post incubation the scaffolds were thawed at room temperature. The scaffolds were treated with sodium borohydride ($NaBH_4$) (0.1M) solution for 2 hours to remove unreacted glutaraldehyde, followed by further washing with deionized water. Post-washing the scaffolds were freeze dried and stored until further use.

Neat PTMC and PTMC+HA and PTMC+TCP circular flat films approx. 1 cm × 0.5 mm in dimension were casted by spread coating the previously developed polymer/ceramic composite resins on glass slides and exposing them to UV (254 nm (UV-C)) light for 40 seconds on either side after covering with a sheet of cellulose acetate film. Post-crosslinking the films were extracted in PC:ethanol (60:40 v/v) gradients to remove solvent as described previously. The films were finally washed 3× with pure ethanol and further dried by placing in vacuum oven at 40 °C for 48 hours for drying, after which the samples were stored in

vacuum desiccator until further used. The films were used for *in vitro* cell material interaction studies post sterilization, as well as XRD studies.

2.4 Characterization of developed scaffolds and films

2.4.1 Microscopy and tomography analysis of scaffolds

The surface features, including surface roughness and particle distribution of the ceramic phase in the SLA fabricated composite scaffolds was evaluated by performing scanning electron microscopy (SEM) using Miniscope TM-1000 (Hitachi, Japan) on the scaffolds. The manufactured scaffolds were imaged using micro-CT (μCT) to analyze the manufacturing quality of the scaffolds. μCT provides a non-destructive method for material characterization. The samples were scanned using Skyscan-1172 (Bruker, Belgium) *ex vivo* μCT system at 50 μA and 50 kV accelerating voltage at pixel size of 5 micron resolution. Overall porosity of the scaffolds was calculated using algorithm available in CTAn software (Bruker, Belgium) after applying suitable thresholding to eliminate microporosities.

2.4.2 Composition analysis of the ceramics and composite scaffolds

X-ray diffraction (XRD) analysis was carried out of synthesized HA and purchased TCP and HA (Sigma, USA) to analyze their phase purity and degree of crystallinity. Further, XRD of the composite films PTMC+HA and PTMC+TCP were also recorded to analyze incorporation of ceramics into the composite materials and effect of the overall fabrication process on purity and crystallinity of the materials.

Thermo-gravimetric analysis (TGA) of the printed 3D scaffolds (PTMC neat, PTMC+HA and PTMC+TCP) was carried out to quantify the incorporation of the inorganic ceramics into the polymer matrices. Samples were heated at rate of 20 ºC/min to a final temperature of 600 °C resulting in total decomposition of the polymer. The residual weight of the material provides information on wt% incorporation of inorganic ceramic in the scaffolds.

2.4.3 Cell material interaction studies

For normal maintenance MC3T3-E1 subclone-4 (mouse calvarial preosteoblasts) were cultured in Minimum Essential Medium Eagle-alpha modification (α-MEM). Human mesenchymal stem cells

(MSCs) (SCC034, Sigma-Aldrich), K7M2 wt (K7M2) (mouse osteoblast) and RAW264.7 (mouse macrophage) cells were cultured in Dulbecco's modified eagle medium (DMEM) at 37 °C in a 95% relative humidity (RH) and 5% CO_2 environment. Before cell seeding, the films were sterilized by placing in 70% ethanol for 4 hours, followed by washing once with phosphate buffered saline (PBS) (1×). The films were incubated in complete medium (10% FBS and 1% penicillin-streptomycin antibiotic) for one hour prior to seeding. For seeding, the cells were trypsinized, checked for viability (trypan blue exclusion assay) and a total of 1×10^4 cells dispersed in 10 µl complete medium were seeded on film surface. The cell seeded films were incubated at 37 °C in a 95% RH and 5% CO_2 environment allowing cells to adhere on film surface for 3-4 hours followed by addition of 500 µl complete media in each well in a 24 well non-treated tissue culture multi-well plate. Cell adhesion and proliferation on surfaces were estimated by performing SEM and fluorescence microscopy analysis of cell seeded films as described elsewhere[51]. Briefly, at day-3 post-seeding, the cells seeded films were washed with PBS (1×), and fixed using paraformaldehyde (4%) solution for 1 hour at 4 °C. For confocal fluorescence imaging (DMi8, Leica-microsystems), the cell nuclei and cytoskeleton (actin filaments) were labelled with 4′,6-diamidino-2-phenylindole (DAPI) and phalloidin-fluorescein isothiocyanate (FITC) respectively. The fixed cells were dried in a desiccator, gold-palladium sputter coated (108auto, Cressington) and imaged using SEM (EVO18, Zeiss) to evaluate cell morphology. To analyze cell proliferation a 3-(4,5-dimethylthiazol-2-yl)-2,5-diphenyl tetrazolium bromide (MTT) assay was carried out on the cell seeded films at regular interval up to day-10 post-seeding.

2.5 Critical size animal bone defect models and *in vivo* implantation studies

The effects of scaffold functionalization with bioactive agents on bone formation and defect healing were initially evaluated in a small pilot study performed using a critical rabbit tibia defect model by implanting unfunctionalized and BMP+ZA functionalized scaffolds. The findings from the pilot tibia study were translated to treat more challenging critical size cranial defects in rabbits. Here, enhanced surface area along with a prolonged release of bioactive agents was provided by infiltrating the SLA scaffolds with macroporous composite cryogel structure. For the tibia defect study, a total of 5 male New Zealand white

rabbits with an age of 5-6 months were used. The rabbits were divided into two groups (Table 1), receiving one defect on each leg. Separately, 23 Belgian white rabbits of age group between 3-4 months divided into 10 groups were used in a cranial defect model with each rabbit receiving four defects (Table 2). Both of the *in vivo* studies and the *in vitro* study groups are visualized also in Figure 1 and the abbreviations used in that figure will be used throughout the rest of this article.

Table 1. Study groups within the *in vivo* tibia defect study.

Group	Treatment	Abbreviation	Nr. of animals	Nr. of defects
G1	PTMC+HA	P-HA	5	5
G2	PTMC+HA+BMP+ZA	P-HA-B-Z	5	5

Table 2. Study groups within the *in vivo* cranial defect study.

Group	Treatment	Abbreviation	Nr. of animals	Nr. of defects
G1	Empty	Empty	2	8
G2	PTMC neat	P	2	8
G3	PTMC+membrane	P+membrane	2	8
G4	PTMC+HA	P-HA	2	8
G5	PTMC+HA+cryogel	P-HA-CG	2	8
G6	PTMC+HA+BMP+ZA	P-HA-B-Z	3	12
G7	PTMC+HA+cryogel+BMP+ZA	P-HA-CG-B-Z	3	12
G8	PTMC+TCP	P-TCP	2	8
G9	PTMC+TCP+cryogel	P-TCP-CG	2	8
G10	PTMC+TCP+cryogel+BMP+ZA	P-TCP-CG-B-Z	3	12

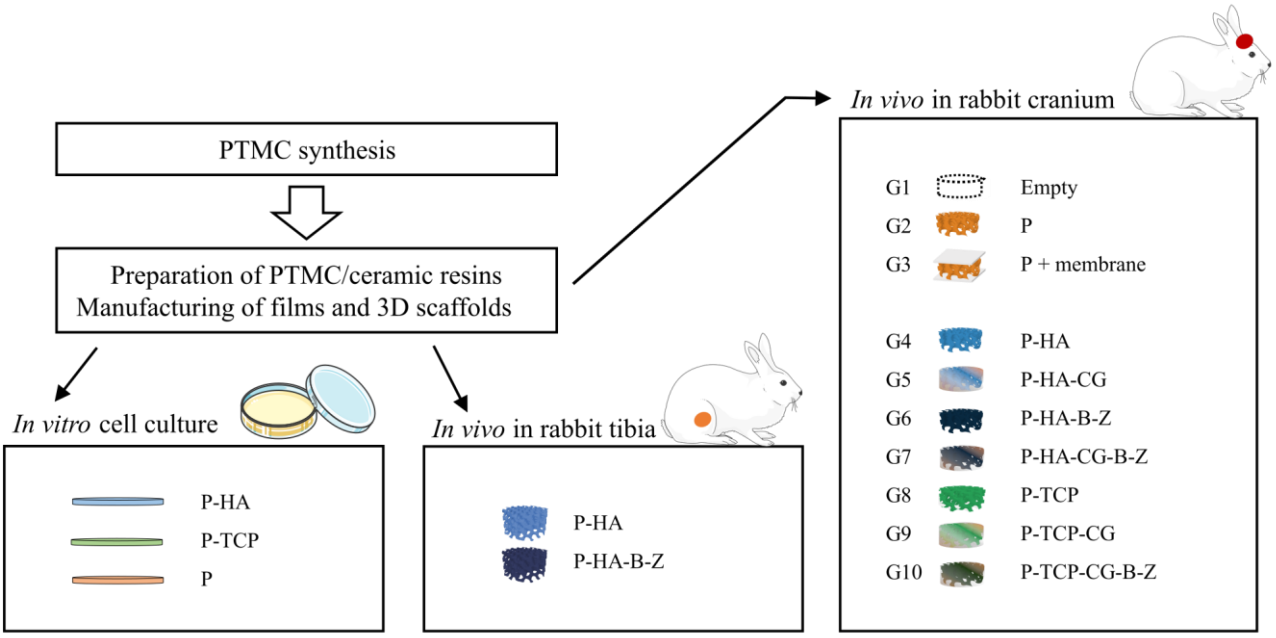

Figure 1. A schematic compiling all the samples described within this work including *in vitro* and *in vivo* studies. The abbreviations are explained in Table 1 and Table 2.

2.5.1 Rabbit tibia long bone defect model

3D printed P-HA scaffolds (10 mm × 5 mm) (diameter × height) were sterilized by placing into 70% ethanol for 6 hours followed by dehydrating them by placing in 100% ethanol for 30 minutes each (3×). The dehydrated scaffolds were further dried in laminar air flow. The scaffolds were either used as such or functionalized with bone morphogenetic protein (BMP) (5 µg/scaffold) + zoledronic acid (ZA) (10 µg/scaffold) to prepare P-HA-B-Z scaffolds. Functionalization was done by surface adsorption of the bioactive molecules from aqueous solution (50 µl) at 4°C for 12 hours. The rabbits were anesthetized with isoflurane using 4% induction and 3% maintenance dose in medical grade oxygen. All animals received prophylactic antibiotic ceftriaxone (40 mg/kg) and analgesic tramadol (5.0 mg/kg). The region near knee joint was cleaned with povidine-iodine and a 2 cm long incision was given along tibia axis exposing the underlying soft tissue. The muscle was removed by blunt cut and underlying periosteum layer covering bone shaft was removed by scrapping. The exposed bone was cleaned using normal saline (0.9% w/v) and a full thickness circular defect (~8.0 mm) was generated by slow cutting under constant saline irrigation using a trephine. Post defect creation the cortical bone was lifted and removed, and the underlying trabecular bone was debrided using as sterile spatula to create a cavity of approximately 5-6 mm to fit the scaffold. The scaffolds were placed into the cavity by applying gentle force so that it is filling the cavity in medullary canal as well as the cortical wall (Figure S1 in Supplementary information). The defect was closed by suturing the overlying skin using 3-0 silk sutures without suturing the periosteum or overlying soft tissue. Post-surgery the animals had free access to food and water *ad libitum* and no further analgesic or antibiotics were given.

2.5.2 Rabbit cranium flat bone defect model

3D printed and cryogel embedded scaffolds (8.0 mm × 2.5 mm) (diameter × height) were sterilized and dried as described above for the tibia study. The scaffolds were either used as such or after functionalization with BMP (5 µg/scaffold) + ZA (10 µg/scaffold) at 4°C for 12 hours. All the study groups are described in Table 2 and Figure 1. In G-3 the implanted scaffolds (P) were covered on top and bottom

with poly(tertafluoroethylene) (PTFE) membrane. The rabbits were prepared for surgery as described previously. After removing hairs from head, the region was treated with povidone-iodine and a full depth skin incision was given starting from frontonasal suture right up to lambdoid suture exposing both frontal and parietal bones. The overlying tissue and periosteal membranes were removed by scraping, exposing the underlying bone. Skin and soft tissue were restrained using retractor and four full thickness circular defects (~8.0 mm) were generated by slow cutting under constant saline irrigation using a trephine on either side of midline with frontal and parietal bones receiving two defects each. Post defect creation the bone was carefully lifted and removed. The cavity was cleared of any remaining bone chunks to prevent injuries/irritation to underlying dura and brain (Figure S2 in Supplementary information). The scaffolds were fit into the cavity by applying gentle force without putting any pressure on underlying brain. The animals received scaffold implantation into the defect according to the groups assigned in Table 2 (see also Figure S2). The defect was closed by suturing the skin using 3-0 silk sutures (Ethicon, India), while the underlying periosteal tissue was not sutured. No further analgesic or antibiotics were given to animals post-surgery. Animals had free access to food and water *ad libitum*.

2.5.3 Radiological and micro-CT analysis of the defects and tissue mineralization

Animals were sacrificed by CO_2 asphyxiation to harvest tibia samples 60-days post-implantation and cranium samples 120 days post-implantation. The samples were immediately fixed in neutral buffered formalin (NBF) (4% w/v) (pH 7.4) for 48 hours at 4°C. Post fixation the samples were washed with deionized water (3×) and incubated in ethanol (70% v/v) at 4°C until further analysis. Digital radiographs for qualitative analysis of tissue mineralization at the defect site were captured using μCT scanner giving single exposure of 3000 ms at 89 kV and 112 μA. *Ex vivo* μCT (Skyscan 1172, Bruker, Belgium) was performed on the samples to analyze tissue mineralization. CT micrographs of tibia samples were recorded using energy settings of 89 kV and 112 μA, with 3000 ms exposure capturing 480 projections, resulting in a voxel size of 11.0 μm. For *ex vivo* CT-analysis on harvested cranium samples, the projections were taken at energy settings of 65 kV, 153 μA with a 6250 ms exposure, capturing a total of 480 projections, with a voxel size of 11.0 μm. A Gaussian-blur (2 pt. radius) filter was applied to the scanned images during

reconstruction. For analysis, all the images were realigned and oriented in same plane (Data viewer, Bruker, Belgium). Quantitative morphometric analysis (CTAn, Bruker, Belgium) was performed on all the samples after applying constant grey value thresholding of 110 on tibia and 125 on cranium samples, respectively. A circular region of interest (ROI) of 8.0 mm diameter and 4.0 mm height in tibia and sufficient height (4-5 mm) in cranium to cover whole of scaffold was analyzed for determining mineralized bone volume (BV), tissue mineralization and scaffold-bone integration.

2.5.4 Histological and analysis of bone formation and defect healing

The fixed and preserved samples were decalcified using Na-EDTA (10% w/v, pH 7.2), before histological analysis. Decalcified tibia samples were longitudinally cut into two, right through the center of the defect, whereas, the cranium samples were transversely cut into two from center of the defect. All the samples were paraffin embedded and sectioned at 7.0 μm thickness for Hematoxylin & Eosin (H&E) and Masson's trichrome (MT) staining. The stained samples were analyzed for tissue infiltration, bone formation patterns and scaffold integration.

2.5.5 Statistical Analysis

All the *in vitro* experiments were carried out in triplicate with the minimum sample size of n = 3. For *in vivo* tibia defect study, the sample size was kept at n = 5 for each group. For *in vivo* cranial defect study, the minimum sample size was kept at n = 8 for all groups with 4 defects in 2 animals. However, the groups employed to evaluate effects of bioactive molecule functionalized scaffolds sample size was at n = 12 with 4 defects in 3 animals. One animal from the P+membrane group died 3-days post implantation due to unknown causes making n = 4 for that group. Statistical differences between groups were determined using one-way ANOVA with Tukey posthoc analysis and two-tailed t test, $\alpha = 0.05$.

2.5.6 Ethics Statement

All the animal procedures were performed by following CPCSEA and IAEC guidelines, using approval number IITK/IAEC/2018/1084. All possible precautions and care were taken to reduce animal sufferings.

3. Results

3.1 Synthesis and characterization of poly(trimethylene carbonate) macromer and resins

A two-step reaction mechanism was used for synthesis of a three-armed PTMC-tMA macromer with methacrylate end groups suitable for photo-crosslinking. The reaction was monitored with ^{1}H NMR based on which monomer conversion, the number-average molar mass (M_n) and the degree of functionalization were calculated [46]. The synthesized oligomer had an average M_n of 10600 g/mol while achieving a monomer conversion ratio of 99%. The degree of functionalization of the PTMC-tMA macromer was 99%. Post-extraction and drying, the macromer was a colorless highly viscous semisolid.

Resins for stereolithography were prepared by dissolving PTMC-tMA in propylene carbonate and adding a photoinitiator. Incorporation of a dye (Orasol Orange) into the resin allows control over the light penetration depth in the resin resulting in user controlled crosslinking [56]. The resins were stable towards sedimentation of the dispersed particles even after letting the resins stand for a long time.

3.2 Characterization of developed scaffolds and films

Following successful additive manufacturing of the polymer/composite scaffolds using stereolithography, the scaffolds were extracted to remove solvent, unreacted photoinitiator, and uncrosslinked polymer and subsequently dried. Scaffolds were sterilized with ethanol, dehydrated, dried and then either used as such or filled with a cryogel prior to implantation. The macroporous composite cryogel provides large surface area and osteoconductive surface for progenitor cell infiltration and differentiation.

3.2.1 Microscopy and tomography analysis of scaffolds

The manufactured scaffolds were scanned at 5 μm resolution using μCT to evaluate the built dimensions compared to the design. Furthermore, the surface of the scaffolds was characterized with scanning electron microscopy (SEM) to evaluate the surface architecture. 3D reconstructions of the manufactured scaffold can be seen in Figure 2. The scaffolds were designed with an overall porosity of 76%, while the manufactured scaffolds had an overall porosity of 75% for PTMC neat and 70-73% for composite

scaffolds. The overall porosity observed for the composite scaffolds infiltrated with cryogels was ~40%, having a uniform interconnected porous architecture as calculated using µCT based algorithmic analysis.

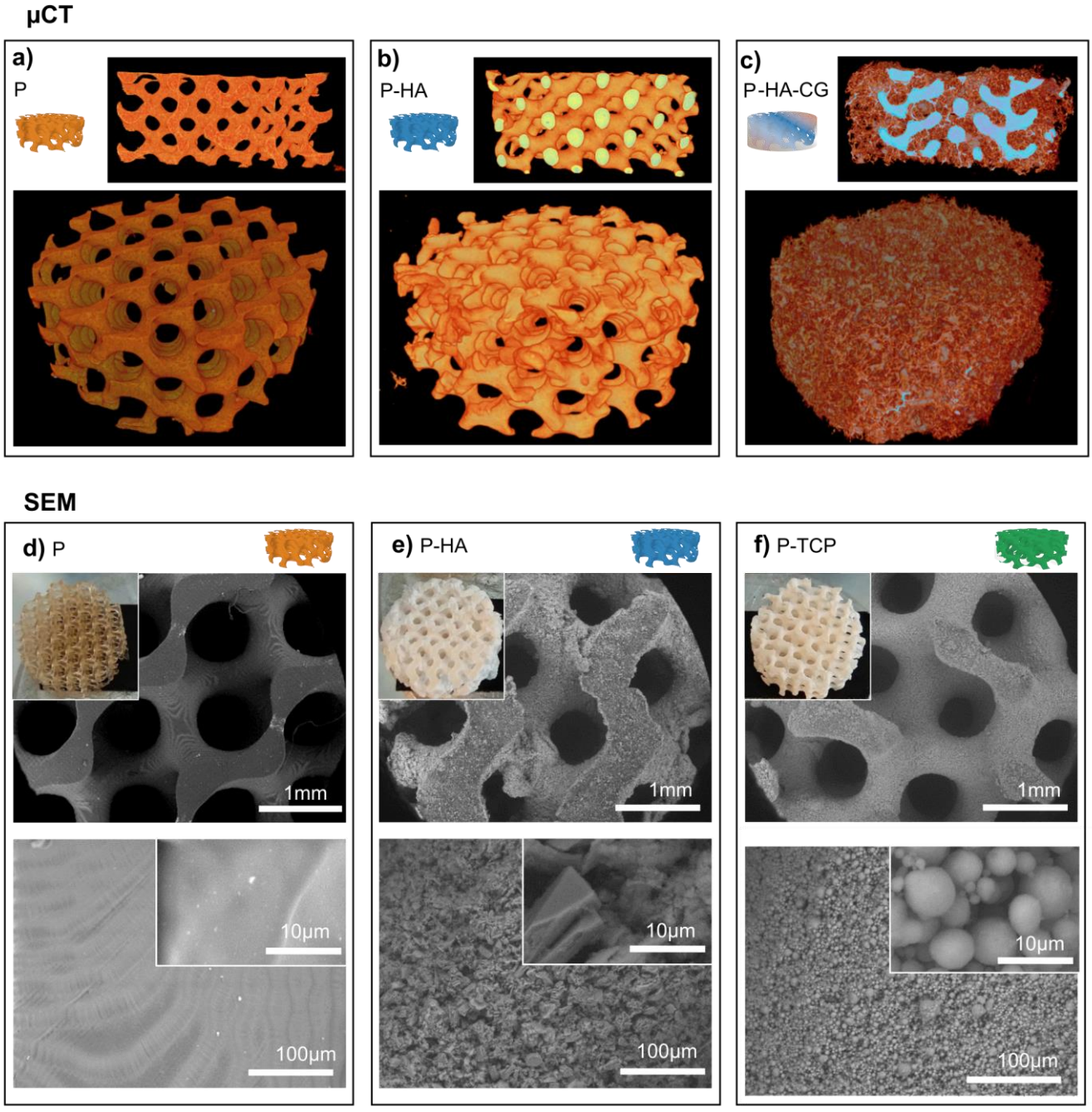

Figure 2. Structural and surface characterization of scaffolds. (a)-(c) Images of the fabricated scaffold 3D models rendered based on µCT including (a) PTMC, (b) PTMC+HA and (c) PTMC+HA+cryogel scaffolds. (d)-(f) SEM micrographs of printed scaffolds showing the smooth polymer surface of a neat PTMC scaffold (d), compared to needle shaped asymmetric HA particles on the surface of the P-HA scaffold (e) and round TCP particles on the surface of the P-TCP scaffold (f).

The high resolution SEM micrographs in Figure 2 show the contoured architecture resulting from the individual layers formed during the printing of the neat PTMC samples. While the neat PTMC scaffold

had a smooth polymer surface, the composites containing HA or TCP revealed a rough surface of composite matrix composed of round TCP and asymmetric needle shaped HA particles embedded in matrix, increasing the overall surface roughness of the composite surfaces.

3.2.2 Composition analysis of the scaffolds

The physicochemical composition of the scaffolds was evaluated by performing x-ray diffraction (XRD) and thermogravimetric analysis (TGA) of the ceramics (HA and TCP), polymer (PTMC) and composites (PTMC+HA or TCP). The results from these measurements can be seen in Figure 3. TGA analysis of the 3D printed neat PTMC scaffolds demonstrated a complete decomposition (residual mass 0.4%) and a degradation temperature around 300°C. Based on the results from the composite scaffolds the ceramic content was calculated. The composite scaffolds revealed residual masses of 54±1% and 53±1% for PTMC+HA and PTMC+TCP scaffolds, respectively corresponding to their ceramic content. In Figure 3b the peaks for the crystalline ceramics are clearly visible in the composite samples comprised within the amorphous polymer.

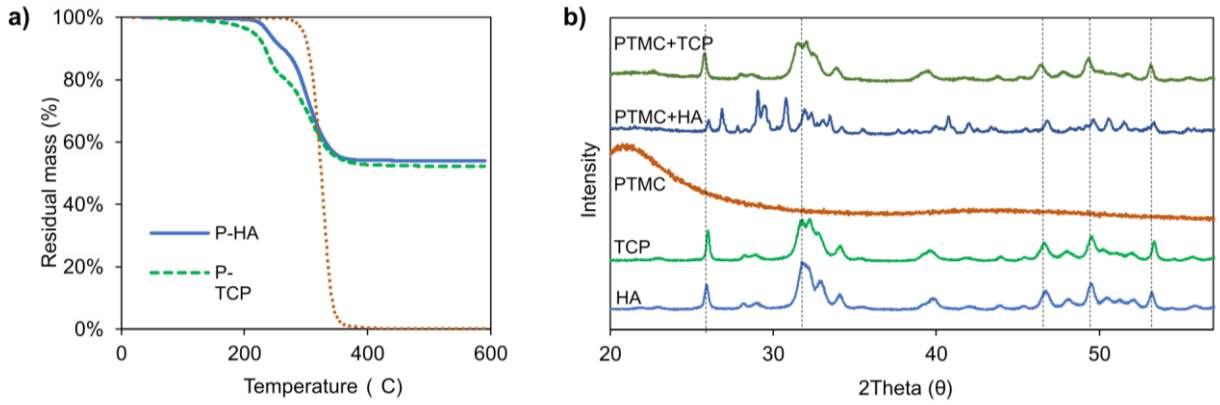

Figure 3. Physicochemical characterization of scaffolds. (a) Representative TGA plots of printed scaffolds showing mass loss as a function of temperature. (b) XRD spectra of the individual ceramics and composite films demonstrating presence of specific ceramic components in composite materials with absence of crystalline phases in neat PTMC. HA in the composite was synthetized in lab, while the individual HA was purchased. TCP was the same grade in both the composite and the individual sample.

3.2.3 Cell material interaction studies

To evaluate the biocompatible behavior of polymer and composite blends *in vitro* cell material interaction and viability studies were performed. Through SEM and fluorescent microscopy, it was observed that PTMC itself and the composites developed thereof were highly biocompatible, supporting cell adhesion

and proliferation, as was observed by cells growing with highly extended and well spread morphologies on material surfaces at day-3 post seeding (Figure 4). Further, the presence of metabolically viable K7M2 osteoblasts cells was observed through positive MTT assay up to day-10 post culture confirming the biocompatible nature of composites supporting cell growth. While cell growth on P and P-HA scaffolds was almost equal, it was less on P-TCP surfaces (Figure S5).

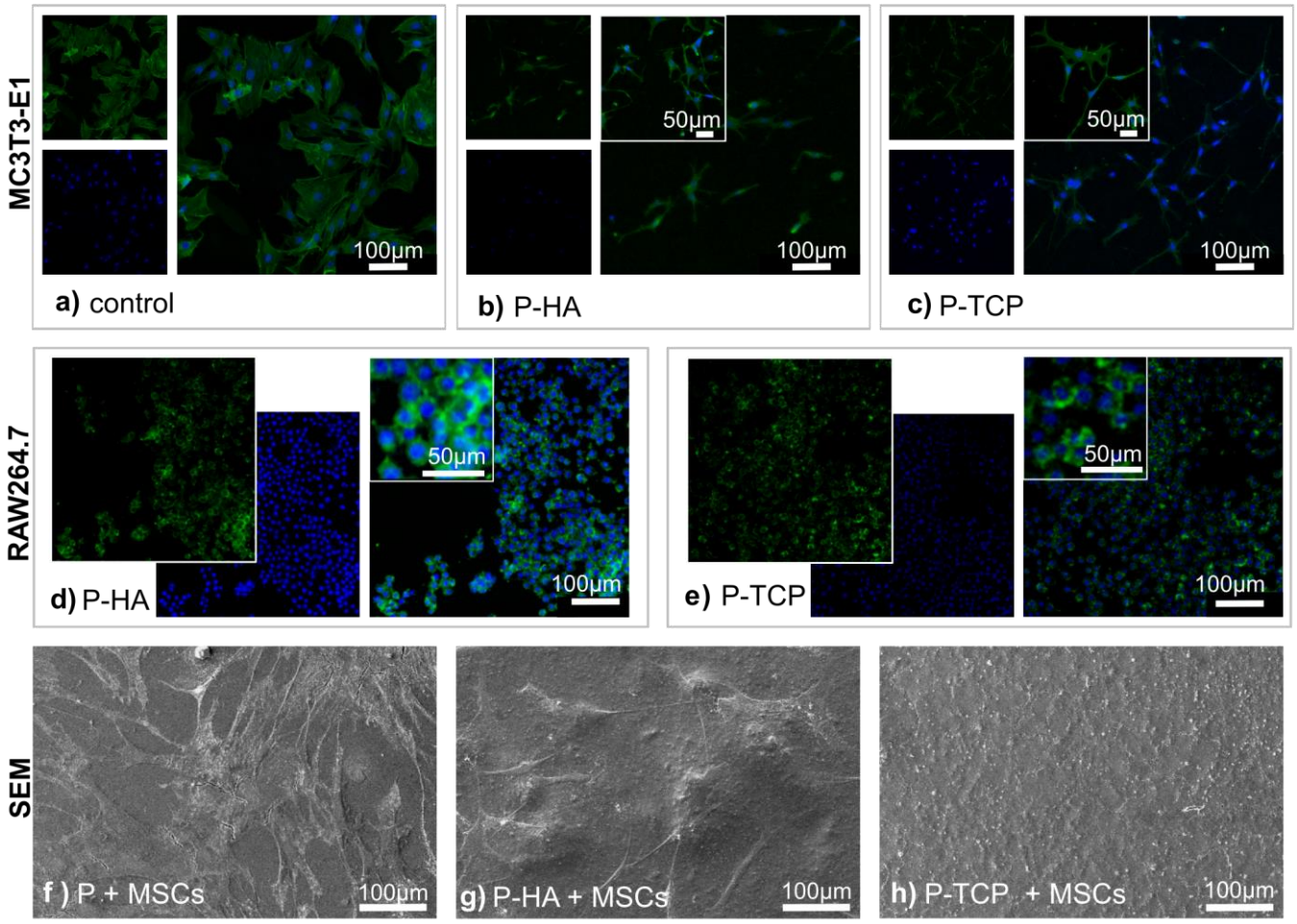

Figure 4. Cell material interaction. (a)-(e) Fluorescence images representing both FITC (green) and DAPI (blue) staining of MC3T3-E1 and RAW264.7 cells on tissue culture plastic (control) and respective material surfaces. The control (a) is tissue culture plastic. Visualized is also a merged image containing both stainings with zoomed portion of image (inset). (f)-(h) SEM imaging of human MSCs cultured on material films showing cell morphologies.

3.3 *In vivo* implantation and mineralization studies in bone defect models

We examined *in vivo* bone formation in rabbits, separately both in long bone (tibia) and flat bone (cranium) critical defect models. Study groups were designed to specifically analyze effects of scaffold implantation *versus* empty defect, and that of functionalization of the scaffolds with BMP and ZA for local delivery on

overall bone formation (Table 1 & 2). Bone formation was evaluated 60-days and 120-days post-implantation in the tibia and cranium models, respectively.

3.3.1 Radiological and µCT analysis for tissue mineralization

Bone formation was assessed by performing *ex vivo* radiological gross imaging and quantitative µCT analysis (Figure 5) of the harvested bone samples. The µCT analysis of tibia samples provided information about the implant site displaying the implanted scaffolds with intact architecture surrounded by substantial amounts of newly generated bone. No loosening, slippage, or significant degradation of the scaffolds was observed. Both groups demonstrated partial defect bridging. A quantitative analysis of the defect site revealed a bone volume – relative to total volume (BV/TV %) of 9.9±1.5% for the BMP+ZA treated group (P-HA-B-Z), while the same value for the P-HA group was 8.5±0.7%. Out of the total void volume, 25% is occupied by the scaffold leaving 75% available for bone infiltration.

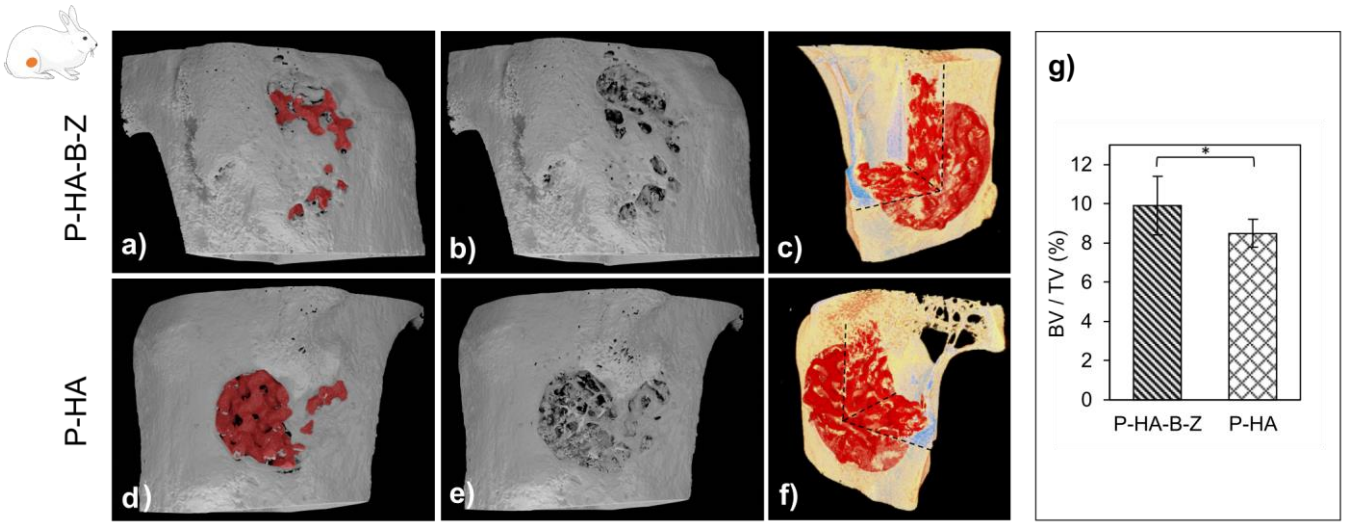

Figure 5. Bone formation analysis in tibia defects. (a)-(f) representative µCT 3D reconstructions of the tibia defect, with implanted scaffolds colored red in (a), (d). The sectioned images of scaffolds display implantation within the defect with bone (light brown) infiltrating within the scaffolds (c) and (f). The scaffold has been removed in (b) and (e) showing bone infiltration pattern within the defect. In (g) the bone volume (BV) relative to the total volume (TV) within the scaffolds is shown for both study groups (mean±SD, n=5, two tailed t test, $\alpha = 0.05$).

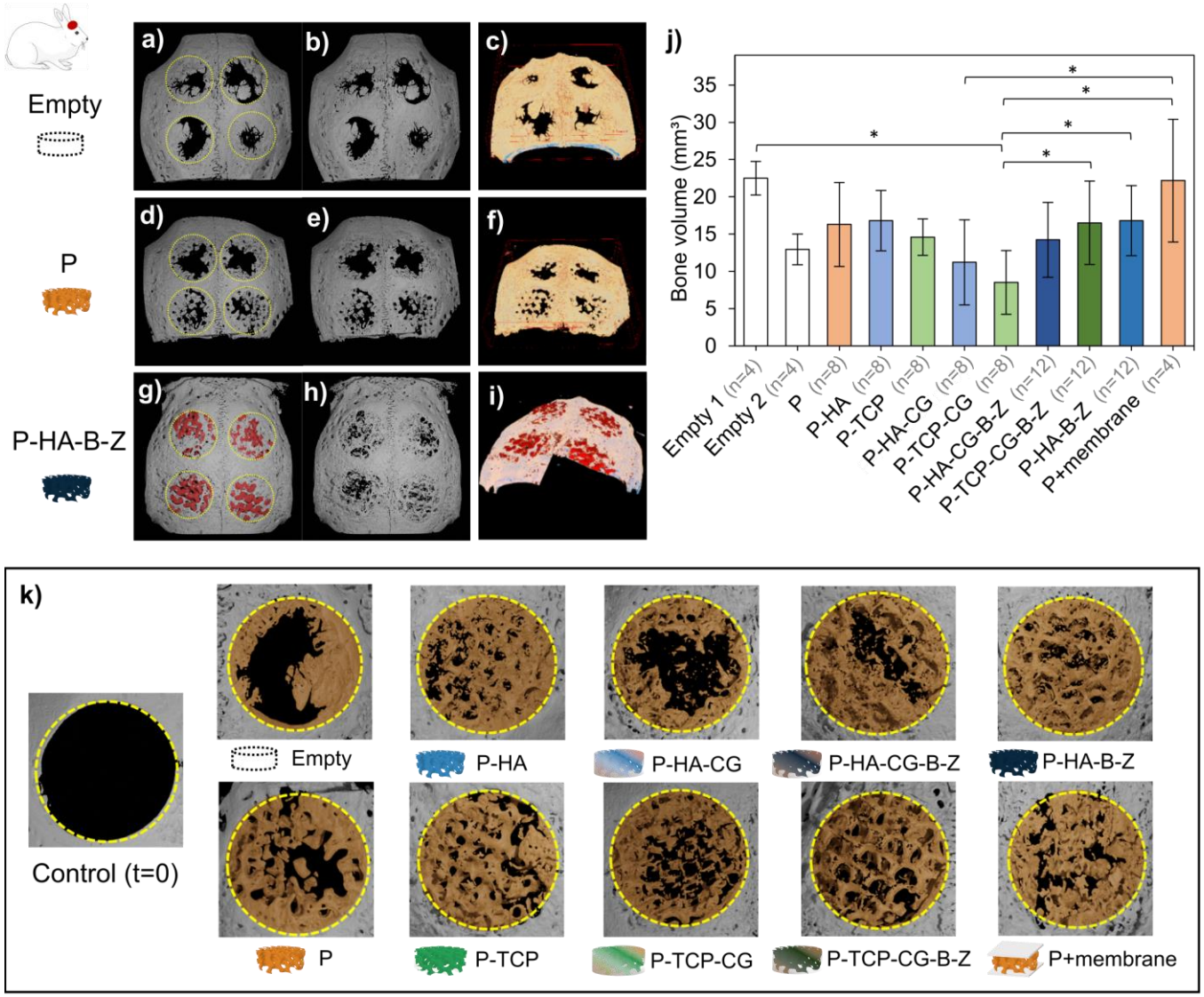

Figure 6. Bone formation analysis of cranial implants. (a)-(i) µCT 3D rendered images representing defect margins (yellow circles) and implanted scaffolds in three groups. The scaffolds are visualized in red or have been removed by thresholding to show tissue mineralization. (j) Bone volume within the defects in all groups presenting averages ± standard deviation. (k) Representative defects from each group showing mineralized tissue depositions and defect healing 16 weeks post-implantation. More defects are visualized in Figure S4.

In µCT analysis (Figure 6) and x-ray analysis (Figure S3 in Supplementary information) of cranium samples, incomplete defect healing and bone infiltration occurring from periphery with large void space still present towards the interior of the defect were observed in non-treated empty group. One of the animals in the empty group behaved unexpectedly, with two of the defects demonstrating almost complete bridging, resulting in higher bone volume (BV) values. In contrast, the study groups treated with implanted scaffolds exhibited higher amounts of mineralized tissue infiltration occurring almost throughout the scaffold, filling most of the void space. Mineralized tissue deposition patterns were more clearly observed on µCT analysis, after removing the scaffolds from the defects (Figure 6h). Here also

slightly higher amounts of mineralized tissue deposition can be observed in composite scaffold groups in comparison to either empty or neat PTMC groups as shown in Figure 6 and in supplementary information (Figure S4), although no significant differences were observed. Among non-functionalized composite groups, HA-containing scaffolds consistently demonstrated higher BV both with and without cryogel infiltration (P-HA-CG = 11.2 mm^3 and P-HA = 16.8 mm^3) than TCP containing scaffolds (P-TCP-CG = 8.2 mm^3 and P-TCP = 14.6 mm^3). On average, the trabecular number (Tb.N) and trabecular thickness (Tb.Th) was higher in P-HA (Tb.N = 0.32 mm, Tb.Th = 0.19 mm) as compared to P-TCP (Tb.N = 0.27 mm, Tb.Th = 0.18 mm). In the non-functionalized, cryogel infiltrated groups mineralization was lower compared to all other groups. Functionalization of composite scaffolds with BMP and ZA results in BVs similar to those found for P-TCP and P-HA (P-HA-B-Z = 16.8 mm^3, P-HA-CG-B-Z = 14.2 mm^3 and P-TCP-CG-B-Z = 16.5 mm^3). The PTMC group (P) also demonstrated almost equal volume deposition (BV = 16.2 mm^3). However, while the volumetric mineralized tissue infiltration was almost similar, the overall deposition patterns and defect closure differed considerably. The P+membrane demonstrated the highest BV of all groups (BV = 22.2 mm^3), with Tb.N = 0.44 mm and Tb.Th = 0.19 mm.

3.3.2 Histological analysis of bone formation and defect healing

Decalcified tibia sections were subjected to MT (Figure 7) and H&E (Figure 8) analysis. In MT staining collagenous bone tissue gets differentially stained in blue color and can be clearly observed. A structurally intact composite scaffold present at the implant site being infiltrated with marrow tissue and new bone depositing in nodular fashion on the scaffold surface was observed. In comparison to non-functionalized P-HA scaffolds, the mineralized tissue deposition was higher in P-HA-B-Z scaffolds, with proper bridging of the defect. Additionally, the mineralized tissue nodules (blue color) were deposited throughout the surface of the scaffold (yellow arrows) (Figure 7). This pattern of ectopic nodular mineralized tissue deposition was less in non-functionalized scaffolds, only occurring on periphery. The matrix of the small freshly deposited bone nodules was irregular and fusiform, while in relatively large nodules it had lamellar architecture, demonstrating remodeling and maturation.

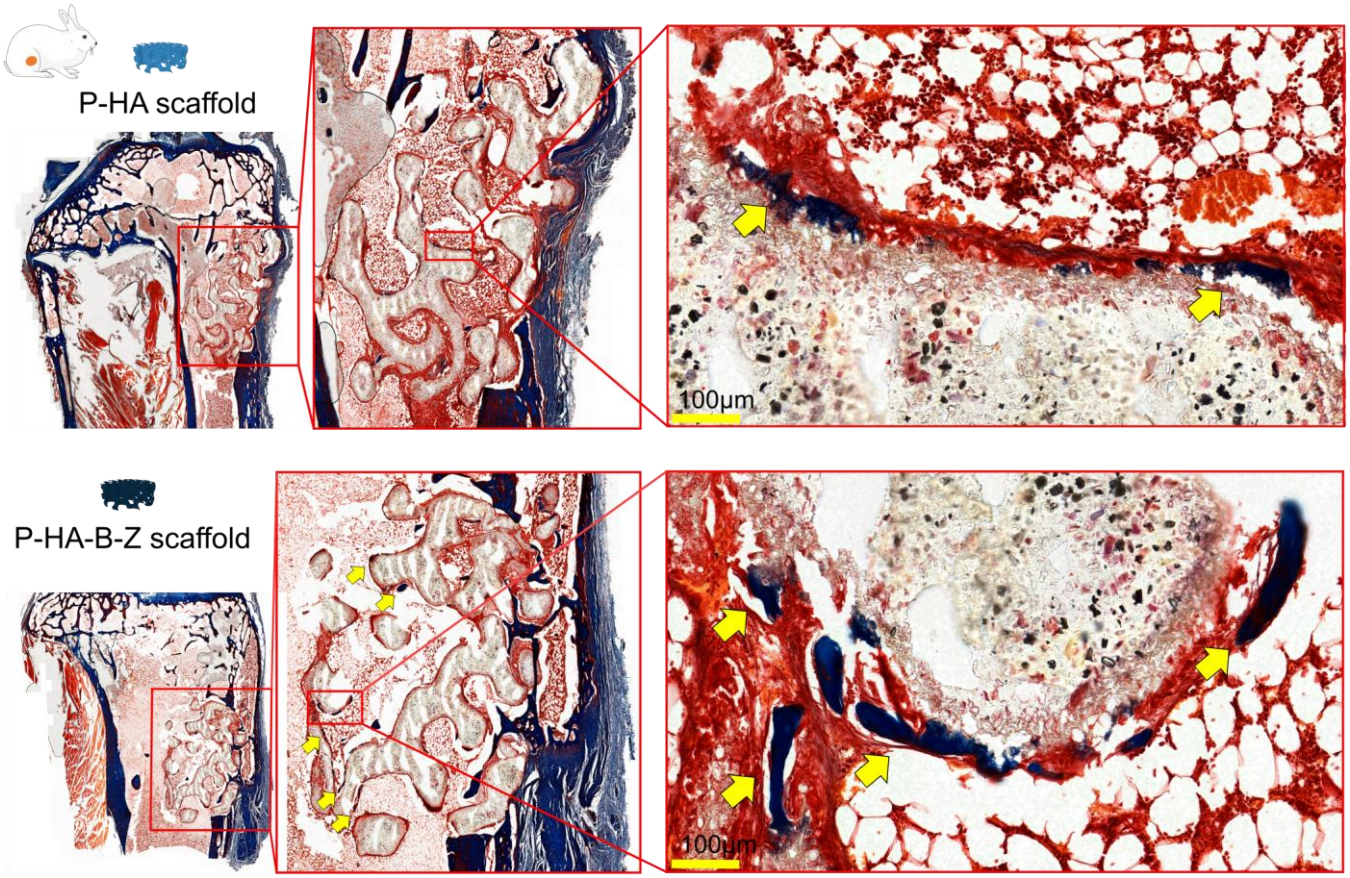

Figure 7. Masson's trichrome staining analysis of bone tissue formation in tibia defects. Yellow arrows are marking the infiltrated osteoblasts and mineralized tissue deposited on the scaffold surface. The scaffold is providing a conductive surface for cell infiltration and bone formation at interior parts of the defect at independent sites.

In the cranium study, the composite scaffolds surpassed PTMC neat (P) and empty defect groups in both continuous and nodular mineralized tissue infiltration (deep blue color) (Figure 8), with more homogeneous bone infiltration throughout the defect. Tissue infiltration patterns within the scaffold differed in both PTMC neat scaffold (P) and P+membrane groups. The P+membrane group had higher bone deposition, with a thin layer of bone getting deposited along the membrane surface and further infiltrating within the scaffolds. Both of the cryogel infiltrated composite scaffolds (P-TCP-CG and P-HA-CG) exhibited lower amounts of mineralized tissue infiltration. In comparison BMP+ZA functionalized respective scaffolds demonstrated higher and more uniform mineralization. Among all the test groups, BMP+ZA functionalized composite scaffold (P-HA-B-Z) exhibited the highest amounts, however the mineralization was more uniform in CG-B-Z groups (Figure 8). It can be clearly observed that the CG infiltrated scaffolds had much higher levels of cell infiltration throughout the scaffolds. Similar to the tibia model, in cranium defects the new bone tissue infiltration was occurring over the surface of

the composite scaffolds, with small nodules getting deposited across the scaffolds and much thicker bone infiltrating from the periphery inwards.

Additionally, Hematoxylin & Eosin (H&E) staining revealed cell types and patterns of hard and soft tissue infiltration into the defects (Figure 9 and 10). In the tibia study, in both groups, a highly bone marrow infiltrated and very well-connected medullary canal was observed (Figure 9), with uniform defect bridging and bone infiltration into the scaffold. A more mature mineralized tissue (pink color) with thicker trabecular walls penetrating deeper into the scaffold was observed in P-HA-B-Z implant group compared to the P-HA scaffold group that demonstrated lesser mineralization.

Similarly, the H&E analysis of rabbit cranium sections (Figure 10), reveals that in the control group (empty), fibrous tissue prominently occupied the defect, with minor bone infiltration on peripheral defect margins. Unlike for the control group, defects containing scaffolds in general were filled with higher amounts of mineralized tissue and even the PTMC neat (P) group demonstrated significantly higher bone infiltration on the scaffold surface and within the pores. The incorporation on the bioactive ceramic (P-HA and P-TCP) clearly increased the infiltration of hard tissue compared to the P group, leading to more homogeneous and lamellar mineralization throughout the scaffold with much thicker walls. Slightly less mineralization was observed in the groups infiltrated with cryogels without any functionalization. However, all implants functionalized with bioactive molecules BMP and ZA, especially the P-HA-B-Z group, showed minimal soft tissue infiltration and significantly higher mineralized tissue infiltration compared to the rest of the groups.

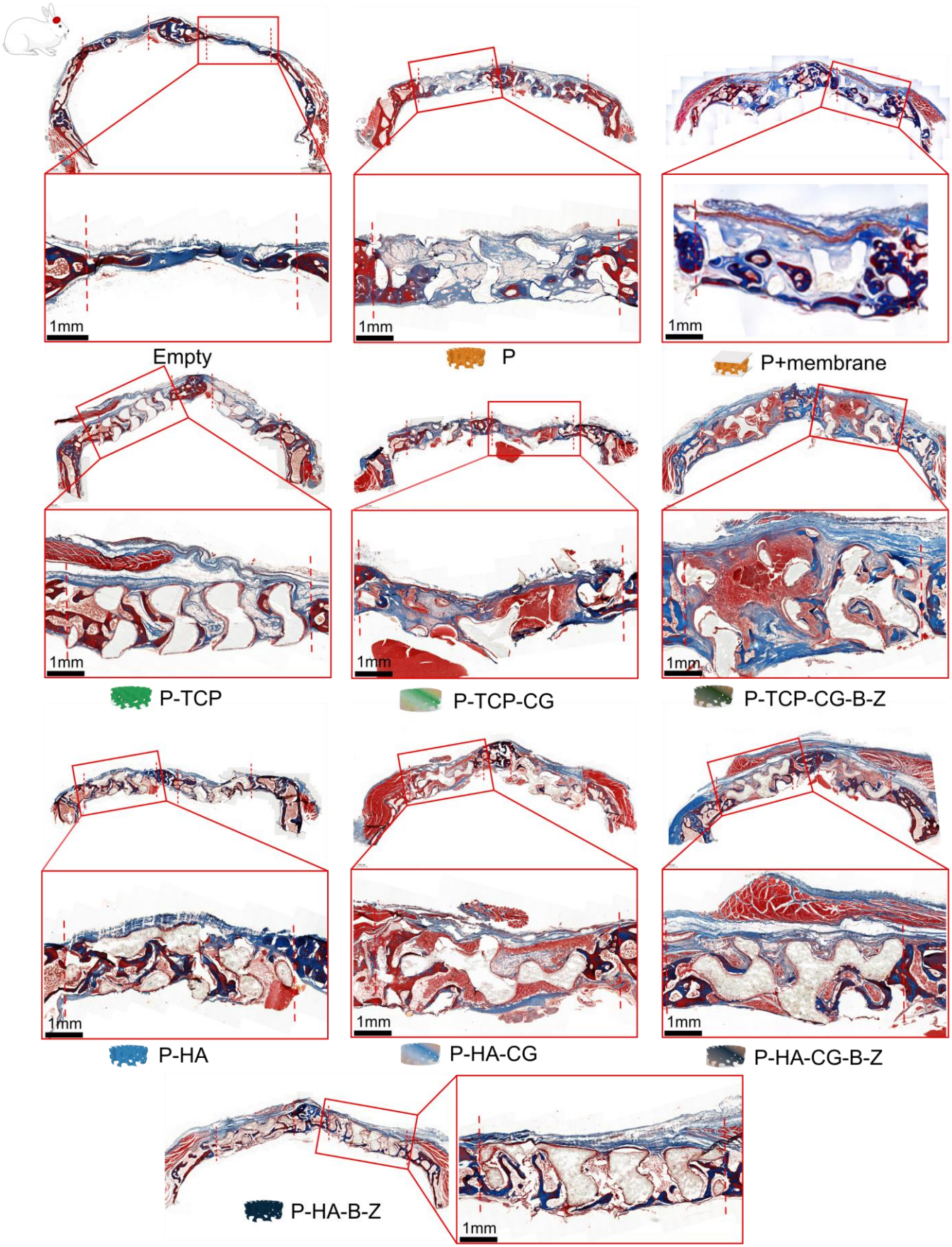

Figure 8. Masson's trichrome staining analysis of bone tissue formation in cranium defects. The samples were transversely cut from the center of the defect therefore showing two scaffolds in the images, one on the left and one on the right of the midline. Additionally, a magnification of one defect is shown. Red dotted lines are representing original defect margins.

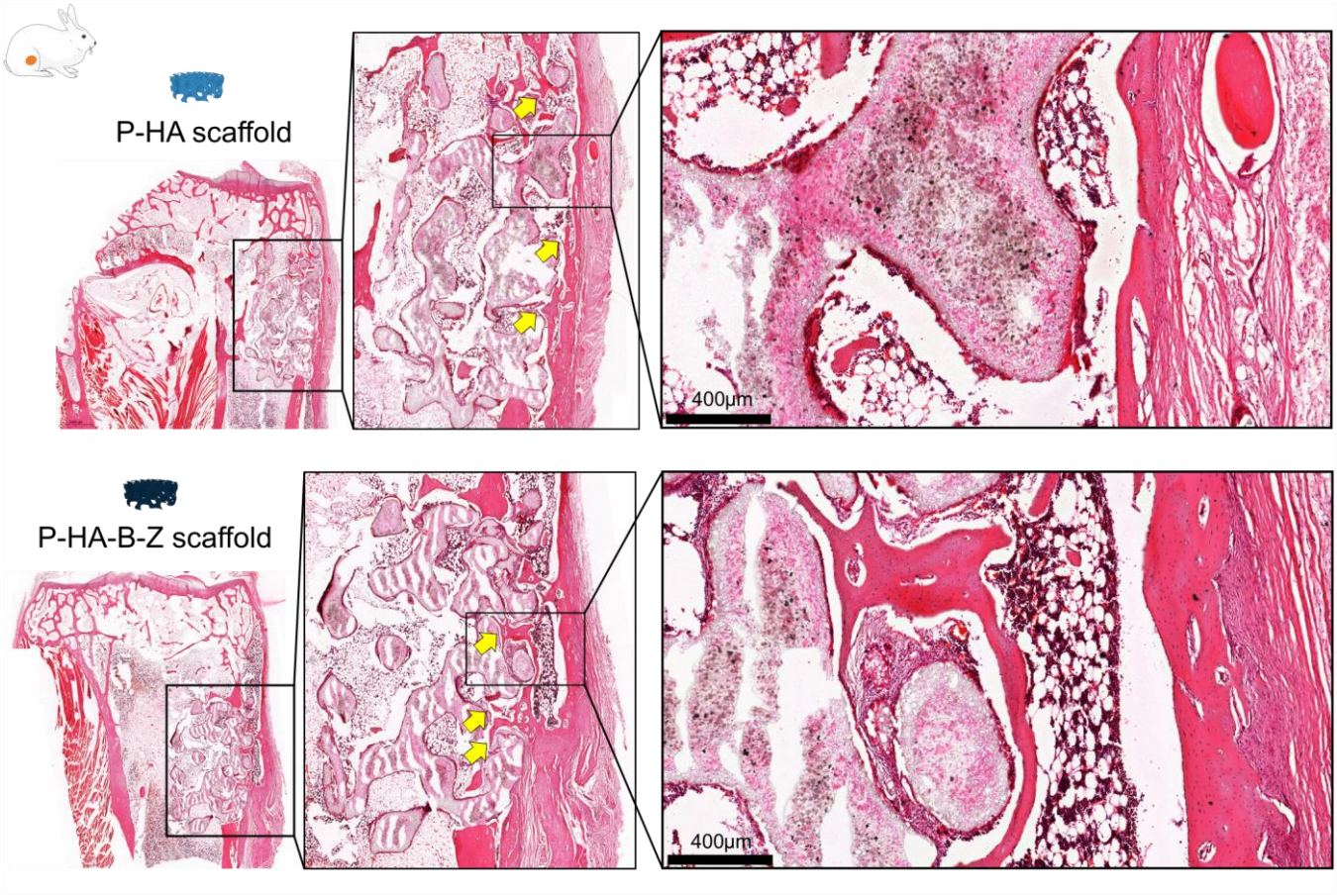

Figure 9. H&E staining analysis of tissue infiltration and bone formation into the tibia defects. Representative images depicting bone marrow and mineralized tissue infiltrating within the scaffolds. Yellow arrows are marking the infiltrated osteoblasts and mineralized tissue deposited on the scaffold surface.

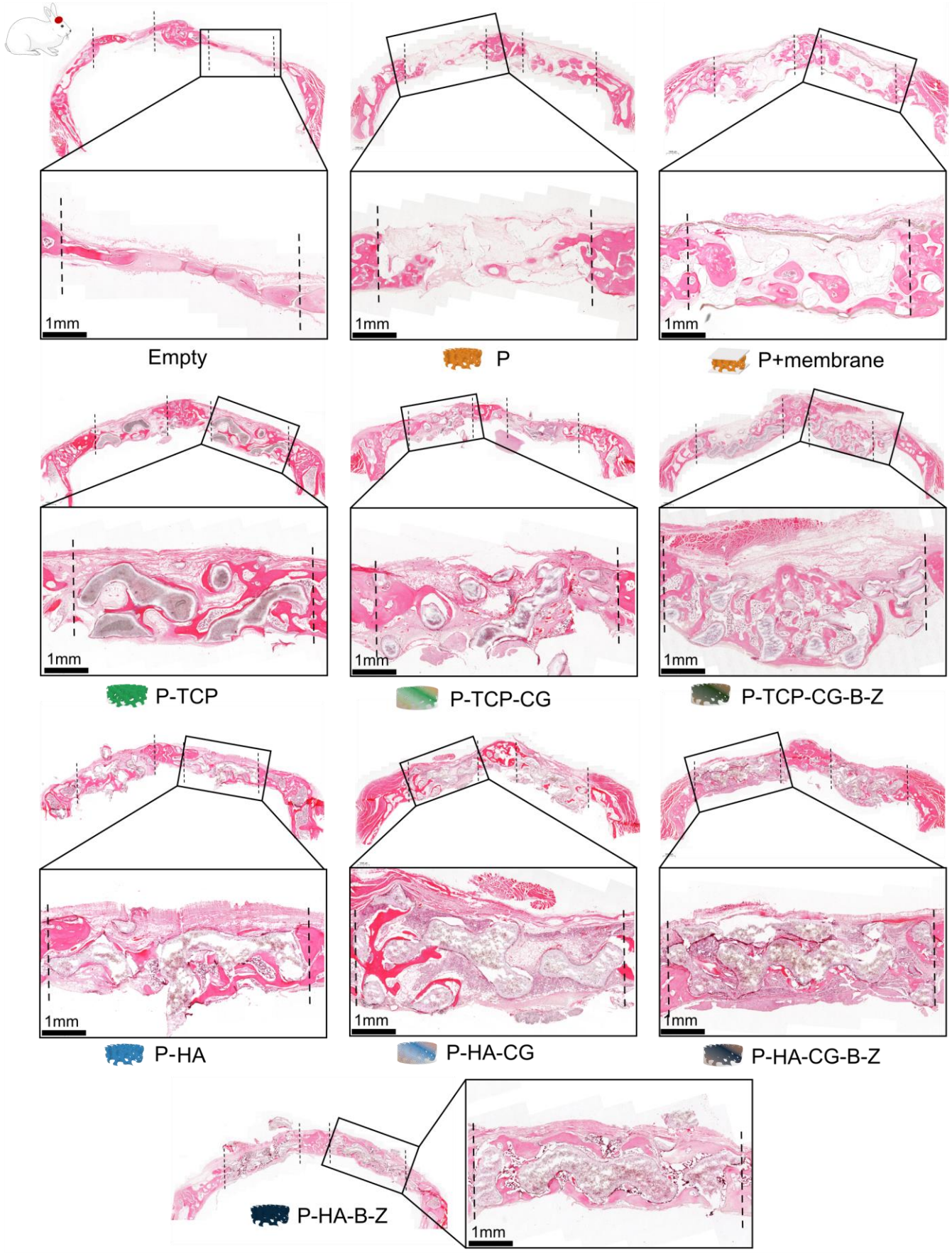

Figure 10. H&E analysis of tissue infiltration and bone formation into the rabbit cranium defects. Black dotted lines are representing original defect margins and the data shows two defects in the cranium with a magnification of one defect.

4. Discussion

The degree of damage and size of the defect, originating due to a traumatic event governs use of an autograft, a support system, or a bone substitute [13,15]. The commonly used bone filler or stabilization materials (metals, polymer cements, and ceramics) have porosity and bio-degradability issues, affecting and often impeding normal tissue healing. Tissue regeneration requires space for cell migration, matrix deposition, and vascularization, which is inhibited by non-porous and non-degradable implants [32,33]. Additionally, the architectural diversity of the bones present in our body rule out a one-for-all solution. Additive manufacturing presents a method allowing control over design parameters such as porosity and architecture, enabling production of individualized implants based on imaging data. In the present study, we fabricated porous PTMC-ceramic (HA or TCP) composite scaffolds for bone regeneration using photocrosslinkable resins and SLA. The composite scaffolds were further infiltrated with respective macroporous composite cryogels (gelatin+HA and gelatin+TCP) to increase the available osteoconductive surface area for cell infiltration while supporting a local controlled release of several bioactive molecules [33,35].

The focus in this study was on biological evaluation including *in vitro* and *in vivo* assessment of the materials and scaffolds developed previously [47], along with examining the effects of bioactive functionalization with BMP and ZA on bone formation. Within this report the developed materials/scaffolds were evaluated using NMR, XRD, TGA, SEM and μCT to verify successful manufacturing and to quantify key physicochemical parameters before biological evaluation. Reconstructions of the scaffolds made from the μCT slides, confirm that the built structures show very close resemblance with the original designed model. This demonstrates the excellent resolution of stereolithography but also validates that the shrinking of the structures during solvent extraction is isotropic. Composition analysis based on TGA revealed a ceramic content of 53-54 wt% in the scaffolds, which is clearly higher than the 40 wt% that was incorporated in the stereolithography resins. However, this was anticipated as similar results have been reported before [47,57]. No phase or crystallinity change were observed in XRD peaks of either HA or TCP composites when compared with pure ceramic

components, depicting mild nature of SLA fabrication process with no degradation effect on the inorganic components.

Both PTMC and composite materials with HA and TCP were highly biocompatible towards different cell lines (MSCs, macrophages, pre-osteoblasts and osteoblasts) during *in vitro* cell viability and biocompatibility studies. The cells adhered well to material surfaces and took extended morphologies as early as 6 hours post seeding as observed through SEM and fluorescent imaging, indicating positive proliferation and cell viability. Positive MTT assay up to day-10 post-seeding further confirmed the biocompatible nature of materials supporting cell growth. Cell growth on both P and P-HA surfaces was almost equal at all the time points. Post day-5, cell proliferation slowed on P-TCP surfaces. This can be potentially due to higher solubility of TCP with regards to HA, affecting cell microenvironment and growth behavior [58], even though TCP is considered highly biocompatible with no known toxic effects. Similar scaffolds have been prepared by our group before, describing the material structure property correlations and indicating that from a material technology point of view a composite scaffold including around 50% ceramic is most favorable for creating patient-specific implants [47]. Furthermore, the biocompatibility of comparable materials have been shown before by others [49,50]. The objective of present study was to enhance the limited osteoinductive properties of ceramic-composite scaffolds by functionalizing them with BMP (5 µg/scaffold) and ZA (10 µg/scaffold), and analyze their *in vivo* applicability. These doses have been found effective for inducing local bone induction and are much lower than the clinically used systemic doses [33,51]. The osteoinductive factors (BMP and ZA) can adsorb on the surface of composites due to their affinity towards incorporated calcium phosphates in addition to being absorbed into the cryogel matrix, providing local delivery of bioactive molecules. BMP and ZA together acts in a synergistic manner, where BMP induced enhanced bone deposition with ZA mediated inhibition of osteoclast mediated resorption leads to net positive bone deposition [51]. Previously we have evaluated performance of ceramics and cryogel composites thereof, and effects of bioactive molecule functionalization on their *in vivo* bone formation activities [32,33]. Here, we tried to integrate the previously developed technologies to augment their performance. We hypothesized that SLA composite scaffolds

will provide a better structural support, whereas cryogel infiltration and functionalization with BMP and ZA, should provide better cell infiltration along with strong osteoinductive signals enhancing overall mineralization.

Cell infiltration and bone supporting capabilities of the scaffolds were evaluated by implanting PTMC neat, P-HA or P-TCP, and bioactive molecule functionalized composite scaffolds into different critical size (~8 mm) defect models in rabbit tibia and cranium separately. The tibia study solely looked at the effect of incorporating BMP and ZA in a composite P-HA scaffold on defect healing. Each rabbit received two defects, one on each leg, with P-HA and P-HA-B-Z scaffolds implanted on opposite legs. The defects healed well during the 60-day trial, as observed through μCT, and the reconstructions made from the harvested bone samples show a clear bridging of the defect in both groups. Although defect bridging was observed in both the implant groups, histology revealed that P-HA-B-Z scaffolds exhibited higher amounts of thick-walled mineralized tissue infiltrating deep into the scaffold from the periphery. Here, deposition of a nodular fusiform mineralized tissue occurring on the surface of scaffolds and further remodeling into mature lamellar bone was observed throughout the scaffold in the Masson's trichrome histological analysis. A phenomenon almost absent in P-HA scaffolds, despite having similar osteoconductive surfaces indicating lack of osteoinductive cues in the latter. Mineralized tissue deposition analysis via μCT further validated our observation, where the P-HA-B-Z group with 9.9±1.5% mean BV/TV % surpasses the P-HA group demonstrating a mean of 8.5±0.7% in quantitative mineralized tissue deposition. An observation further confirming effects of osteoinductive cues on scaffold performance.

In the rabbit cranial study lasting 120-days, a total of 10 groups were analyzed. Alike in the long bone, treatment groups that received bioactive molecule (BMP + ZA) functionalized composite scaffolds, exhibited higher amounts of mineralized tissue deposition compared to non-functionalized scaffolds. The empty defects were prominently occupied with fibrous tissue with incomplete void filling and defect bridging. However, significantly higher bone infiltration was observed even within neat PTMC scaffolds (P). The porous scaffold shields the defect site while providing a guiding surface with a large surface area

for tissue ingrowth. This can be noted by observing the patterns of bone infiltration. A similar trend but with higher mineralization was observed when the PTMC scaffolds were covered on both top and bottom of the defect with a thin PTFE membrane to inhibit cell infiltration from the overlying periosteum (the periosteum was not sutured). This demonstrates that bone infiltration is occurring by osteoblasts migrating from existing bone margins and the membrane is acting like the periosteum, guiding bone infiltration. We speculate that this bone formation pattern was also responsible for the higher amount of overall bone formation observed in μCT. In this group, higher bone growth occurred both in the scaffold and along the surface of the membrane. Similar results have been presented before when using PTFE membranes to treat defects in rat mandible [59].

Comparatively, the composite scaffolds, including HA or TCP, exhibited similar amounts of total mineralized tissue infiltration, but the infiltration patterns and extent were different. In the composite scaffolds the bone formation was more dispersed throughout the scaffold, indicating the presence of a more osteoconductive surface. Among P-TCP and P-HA groups almost similar patterns in bone infiltration were observed, with HA filled scaffolds generally performing slightly better than the TCP equals. We speculate this can be due to early resorption of more soluble TCP [60] form the surface of the scaffolds as compared to the almost insoluble HA. The rapidly solubilizing TCP can lead to a change in local pH of the scaffold surface microenvironment affecting cell proliferation. Similar results were observed during *in vitro* cell studies on P-TCP and P-HA films, where also cell proliferation on P-TCP was lower than on P or P-HA. Although quantitatively in this study the composites performed as well as the neat PTMC scaffolds, the ceramic composites can be considered as far better bone scaffolds due to the improved mechanical properties achieved through the addition of bone mimicking calcium ceramics.

In an attempt to further increase the surface area of the scaffold, they were infiltrated with composite cryogels incorporated with the same ceramics as the scaffolds themselves. Although there was a higher amount of the cell infiltration, these groups had less mineralized tissue. The infiltration of the scaffolds with composite cryogel lead to an overall decrease in porosity of the scaffolds from 75% to 40%. Our interpretation is that this decreased porosity, in absence of strong inductive cues, can obstruct cell

infiltration, therefore reducing the new bone deposition in these cryogel infiltrated scaffolds. However, when the same cryogel filled scaffolds were functionalized with bioactive molecules (P-HA-CG-B-Z and P-TCP-CG-B-Z), it enhanced bone deposition as could be observed in both μCT and histology analysis. We speculate that the presence of limited amounts of ceramics on the surface of P-HA restricts the amount of bioactives getting loaded affecting the overall outcome for P-HA and P-HA-B-Z and making them perform equally. However, comparatively larger amounts of bioactives can get absorbed into the cryogel matrices, which explains why functionalized cryogel infiltrated group performed better than their corresponding non-functionalized groups. This observation supports that the presence of osteoconductive surfaces along with strong osteoinductive cues (BMP+ZA) positively influences the cell differentiation and mineralized tissue deposition.

SLA manufactured PTMC+HA composites have been shown to be biocompatible and osteoconductive [49,50]. PTMC neat scaffolds manufactured by SLA are highly elastic, with a low stiffness and therefore do not provide an optimal support. However, PTMC networks provide an excellent matrix for composites as the flexibility of the network allows for incorporation of considerable quantities of osteoconductive ceramics that in addition extensively reinforces the matrix. Incorporation of high amounts of ceramic components (> 40 wt%) enhances their stiffness making them more rigid to deformation, and therefore better for protecting the underlying soft brain if used to support healing of the cranium. A suitable stiffness provided by ceramics also induces differentiation of progenitor cells into osteogenic lineage (osteoinduction) [61]. Additionally, the enzymatic surface degradation of PTMC maintains mechanical properties for appropriate time providing support structure for bone growth [42,50]. This study confirms that P-HA or P-TCP composites have an excellent conductive surface. Moreover, it builds on previous work by improving the bone regeneration properties of those scaffolds by means of functionalization with osteoinductive molecules (BMP and ZA), while demonstrating that the scaffolds enable adsorption of said molecules. We also observed that presence of a guiding surface and macroporous architecture significantly influences cell infiltration, remodeling and bone healing activities. By combining these unique

characteristics the overall bone substitute properties were increased, resulting in higher mineralized tissue infiltration as shown in this study.

5. Conclusions

The study provides strong evidence in favor of 3D printed composite materials as synthetic bone substitutes. These materials can be fabricated into patient specific dimensions and architectures with controlled porosities. We successfully demonstrated the osteoconductive surfaces of SLA fabricated composite scaffolds. Furthermore, we improved the overall osteoinductivity of the scaffolds through functionalization with BMP and ZA, as observed by enhancement in bone formation efficiency of the functionalized scaffolds *in vivo*. A carrier mediated site specific controlled delivery of these molecules using such matrices can decrease their required therapeutic doses, overcoming in-efficient delivery related side effects. We observed that the presence of a scaffold, along with a guiding membrane and bioactives, can positively influence bone deposition. Our findings provide strong evidence in favor of stereolithography fabricated bioactive molecule functionalized composites as next generation patient specific bone substitute solutions.

Supporting Information

Supporting information: schematic representing generation of critical size defect in tibia (Figure S1) and cranium (Figure S2); representative radiological images of cranial implant in rabbits (Figure S3); 3D Rendered μCT images of cranial implants (Figure S4); MTT cell viability analysis (Figure S5).

Author Contributions

AK, JS, AKT, KD and IQ designed the whole study. AKT and KD developed and characterized the materials with inputs from BB. AKT, IQ and SG performed cell studies, animal surgery and histology. AKT and IQ carried out μCT sample scanning and AKT and KD performed the ex vivo μCT analysis. AKT and IQ wrote the manuscript draft along with KD and BB. The manuscript was further reviewed by all co-authors.

Acknowledgements

The authors would like to acknowledge the Department of Biotechnology (DBT), Ministry of Science and Technology, Government of India for majorly funding this research project (Project# BT/IN/Sweden/08/AK/2017-18). The authors also acknowledge the partial funding from the Department of Science and Technology (DST), Ministry of Science and Technology (Project# DST/INT/SWD/P-11/2016 and Project# DST/NM/NT-2018/48) and Ministry of Human Resource Development (MHRD) and Indian Council of Medical Research (ICMR) funded Uchhatar Avishkar Yojana (UAY) scheme (Project# MHRD_IITK_006), MHRD-IMPRINT (MHRD_6714/Healthcare), MHRD-SPARC (SPARC/2018–2019/P612/SL), Govt. of India. AKT would like to acknowledge MHRD, Govt of India and Indian Institute of Technology Kanpur for providing the research fellowships and Aalto University for research visit to Aalto University, Finland. IQ and SG would like to acknowledge MHRD, Govt of India and Indian Institute of Technology Kanpur for providing the PhD fellowship. AK acknowledges Rajeeva and Sangeeta Lahri Chair Fellowship. This work made use of Aalto University Bioeconomy Facilities. Histology images were generated using 3DHISTECH Panoramic 250 FLASH II digital slide scanner at Genome Biology Unit supported by HiLIFE and the Faculty of Medicine, University of Helsinki, and Biocenter Finland.

References

(1) Jeyaraj, P. Cranial Vault Defects and Deformities Resulting from Combat-Related Gunshot, Blast and Splinter Injuries: How Best to Deal with Them. *J. Maxillofac. Oral Surg.* **2019**. https://doi.org/10.1007/s12663-019-01258-1.

(2) Hassanein, A. G. Trends and Outcomes of Management of Mandibular Fractures. *J. Craniofac. Surg.* **2019**, *30* (4), 1245–1251. https://doi.org/10.1097/SCS.0000000000005469.

(3) El-Rashidy, A. A.; Roether, J. A.; Harhaus, L.; Kneser, U.; Boccaccini, A. R. Regenerating Bone with Bioactive Glass Scaffolds: A Review of in Vivo Studies in Bone Defect Models. *Acta Biomaterialia*. Acta Materialia Inc October 15, 2017, pp 1–28. https://doi.org/10.1016/j.actbio.2017.08.030.

(4) Einhorn, T. A.; Gerstenfeld, L. C. Fracture Healing: Mechanisms and Interventions. *Nat. Rev. Rheumatol.* **2014**, *11* (1), 45–54. https://doi.org/10.1038/nrrheum.2014.164.

(5) Ghiasi, M. S.; Chen, J.; Vaziri, A.; Rodriguez, E. K.; Nazarian, A. Bone Fracture Healing in Mechanobiological Modeling: A Review of Principles and Methods. *Bone Reports* **2017**, *6*, 87–100. https://doi.org/10.1016/j.bonr.2017.03.002.

(6) Nakajima, A.; Nakajima, F.; Shimizu, S.; Ogasawara, A.; Wanaka, A.; Moriya, H.; Einhorn, T. .; Yamazaki, M. Spatial and Temporal Gene Expression for Fibroblast Growth Factor Type I Receptor (FGFR1) during Fracture Healing in the Rat. *Bone* **2001**, *29* (5), 458–466. https://doi.org/10.1016/S8756-3282(01)00604-4.

(7) Tsuji, K.; Bandyopadhyay, A.; Harfe, B. D.; Cox, K.; Kakar, S.; Gerstenfeld, L.; Einhorn, T.; Tabin, C. J.; Rosen, V. BMP2 Activity, Although Dispensable for Bone Formation, Is Required for the Initiation of Fracture Healing. *Nat. Genet.* **2006**, *38* (12), 1424. https://doi.org/10.1038/ng1916.

(8) Chen, Y.; Alman, B. A. Wnt Pathway, an Essential Role in Bone Regeneration. *J. Cell. Biochem.*

2009, *106* (3), 353–362. https://doi.org/10.1002/jcb.22020.

(9) Majidinia, M.; Sadeghpour, A.; Yousefi, B. The Roles of Signaling Pathways in Bone Repair and Regeneration. *J. Cell. Physiol.* **2018**, *233* (4), 2937–2948. https://doi.org/10.1002/jcp.26042.

(10) Ferguson, C.; Alpern, E.; Miclau, T.; Helms, J. A. Does Adult Fracture Repair Recapitulate Embryonic Skeletal Formation? *Mech. Dev.* **1999**, *87* (1–2), 57–66. https://doi.org/10.1016/S0925-4773(99)00142-2.

(11) Vortkamp, A.; Pathi, S.; Peretti, G. M.; Caruso, E. M.; Zaleske, D. J.; Tabin, C. J. Recapitulation of Signals Regulating Embryonic Bone Formation during Postnatal Growth and in Fracture Repair. *Mech. Dev.* **1998**. https://doi.org/10.1016/S0925-4773(97)00203-7.

(12) Li, Y.; Chen, S. K.; Li, L.; Qin, L.; Wang, X. L.; Lai, Y. X. Bone Defect Animal Models for Testing Efficacy of Bone Substitute Biomaterials. *J. Orthop. Transl.* **2015**, *3* (3), 95–104. https://doi.org/10.1016/j.jot.2015.05.002.

(13) Nauth, A.; Schemitsch, E.; Norris, B.; Nollin, Z.; Watson, J. T. Critical-Size Bone Defects: Is There a Consensus for Diagnosis and Treatment? *J. Orthop. Trauma* **2018**, *32* (3), S7–S11. https://doi.org/10.1097/BOT.0000000000001115.

(14) Schemitsch, E. H. Size Matters: Defining Critical in Bone Defect Size! *J. Orthop. Trauma* **2017**, *31* (10), S20–S22. https://doi.org/10.1097/BOT.0000000000000978.

(15) Bonda, D. J.; Manjila, S.; Selman, W. R.; Dean, D. The Recent Revolution in the Design and Manufacture of Cranial Implants. *Neurosurgery* **2015**, *77* (5), 814–824. https://doi.org/10.1227/NEU.0000000000000899.

(16) Kim, J. S.; Cheong, J. H.; Ryu, J. Il; Kim, J. M.; Kim, C. H. Bone Flap Resorption Following Cranioplasty after Decompressive Craniectomy: Preliminary Report. *Korean J. Neurotrauma* **2015**, *11* (1), 1. https://doi.org/10.13004/kjnt.2015.11.1.1.

(17) Brommeland, T.; Rydning, P. N.; Pripp, A. H.; Helseth, E. Cranioplasty Complications and Risk

Factors Associated with Bone Flap Resorption. *Scand. J. Trauma. Resusc. Emerg. Med.* **2015**, *23* (1), 75. https://doi.org/10.1186/s13049-015-0155-6.

(18) Gugala, Z.; Lindsey, R. W.; Gogolewski, S. New Approaches in the Treatment of Critical-Size Segmental Defects in Long Bones. *Macromol. Symp.* **2007**, *253* (1), 147–161. https://doi.org/10.1002/masy.200750722.

(19) Key, J. A. The Effect of a Local Calcium Depot on Osteogenesis and Healing of Fractures. *J. Bone Jt. Surg.* **1934**, *16* (1), 176–184.

(20) Jorgenson, D. S.; Mayer, M. H.; Ellenbogen, R. G.; Centeno, J. A.; Johnson, F. B.; Mullick, F. G.; Manson, P. N. Detection of Titanium in Human Tissues after Craniofacial Surgery. *Plast. Reconstr. Surg.* **1997**, *99* (4), 976–979. https://doi.org/10.1097/00006534-199704000-00006.

(21) Marcián, P.; Narra, N.; Borák, L.; Chamrad, J.; Wolff, J. Biomechanical Performance of Cranial Implants with Different Thicknesses and Material Properties: A Finite Element Study. *Comput. Biol. Med.* **2019**, *109* (November 2018), 43–52. https://doi.org/10.1016/j.compbiomed.2019.04.016.

(22) Golz, T.; Graham, C. R.; Busch, L. C.; Wulf, J.; Winder, R. J. Temperature Elevation during Simulated Polymethylmethacrylate (PMMA) Cranioplasty in a Cadaver Model. *J. Clin. Neurosci.* **2010**, *17* (5), 617–622. https://doi.org/10.1016/j.jocn.2009.09.005.

(23) Ripamonti, U.; Roden, L. C.; Renton, L. F. Osteoinductive Hydroxyapatite-Coated Titanium Implants. *Biomaterials* **2012**, *33* (15), 3813–3823. https://doi.org/10.1016/j.biomaterials.2012.01.050.

(24) Schmidleithner, C.; Malferrari, S.; Palgrave, R.; Bomze, D.; Schwentenwein, M.; Kalaskar, D. M. Application of High Resolution DLP Stereolithography for Fabrication of Tricalcium Phosphate Scaffolds for Bone Regeneration. *Biomed. Mater.* **2019**, *14* (4), 045018. https://doi.org/10.1088/1748-605X/AB279D.

(25) Samavedi, S.; Whittington, A. R.; Goldstein, A. S. Calcium Phosphate Ceramics in Bone Tissue Engineering: A Review of Properties and Their Influence on Cell Behavior. *Acta Biomaterialia*. Elsevier September 1, 2013, pp 8037–8045. https://doi.org/10.1016/j.actbio.2013.06.014.

(26) Shah, A. M.; Jung, H.; Skirboll, S. Materials Used in Cranioplasty: A History and Analysis. *Neurosurg. Focus* **2014**, *36* (4), E19. https://doi.org/10.3171/2014.2.FOCUS13561.

(27) Esmi, A.; Jahani, Y.; Yousefi, A. A.; Zandi, M. PMMA-CNT-HAp Nanocomposites Optimized for 3D-Printing Applications. *Mater. Res. Express* **2019**, *6* (8). https://doi.org/10.1088/2053-1591/ab2157.

(28) Ronca, A.; Ambrosio, L.; Grijpma, D. W. Design of Porous Three-Dimensional PDLLA/Nano-Hap Composite Scaffolds Using Stereolithography. *J. Appl. Biomater. Funct. Mater.* **2012**, *10* (3), 249–258. https://doi.org/10.5301/JABFM.2012.10211.

(29) Kim, S.-S.; Sun Park, M.; Jeon, O.; Yong Choi, C.; Kim, B.-S. Poly(Lactide-Co-Glycolide)/Hydroxyapatite Composite Scaffolds for Bone Tissue Engineering. *Biomaterials* **2006**, *27* (8), 1399–1409. https://doi.org/10.1016/j.biomaterials.2005.08.016.

(30) Vallet-Regí, M.; Ruiz-Hernández, E. Bioceramics: From Bone Regeneration to Cancer Nanomedicine. *Adv. Mater.* **2011**, *23* (44), 5177–5218. https://doi.org/10.1002/adma.201101586.

(31) Geven, M. A.; Varjas, V.; Kamer, L.; Wang, X.; Peng, J.; Eglin, D.; Grijpma, D. W. Fabrication of Patient Specific Composite Orbital Floor Implants by Stereolithography. *Polym. Adv. Technol.* **2015**, *26* (12), 1433–1438. https://doi.org/10.1002/pat.3589.

(32) Teotia, A. K.; Raina, D. B.; Isaksson, H.; Tägil, M.; Lidgren, L.; Seppälä, J.; Kumar, A. Composite Bilayered Scaffolds with Bio-Functionalized Ceramics for Cranial Bone Defects: An in Vivo Evaluation. *Multifunct. Mater.* **2019**, *2* (1), 014002. https://doi.org/10.1088/2399-7532/aafc5b.

(33) Teotia, A. K.; Qayoom, I.; Kumar, A. Endogenous Platelet-Rich Plasma Supplements/Augments

Growth Factors Delivered via Porous Collagen-Nanohydroxyapatite Bone Substitute for Enhanced Bone Formation. *ACS Biomater. Sci. Eng.* **2019**, *5* (1), 56–69. https://doi.org/10.1021/acsbiomaterials.8b00227.

(34) Horstmann, P. F.; Raina, D. B.; Isaksson, H.; Hettwer, W.; Lidgren, L.; Petersen, M. M.; Tägil, M. Composite Biomaterial as a Carrier for Bone-Active Substances for Metaphyseal Tibial Bone Defect Reconstruction in Rats. *Tissue Eng. Part A* **2017**, *23* (23–24), 1403–1412. https://doi.org/10.1089/ten.TEA.2017.0040.

(35) Raina, D. B.; Isaksson, H.; Teotia, A. K.; Lidgren, L.; Tägil, M.; Kumar, A. Biocomposite Macroporous Cryogels as Potential Carrier Scaffolds for Bone Active Agents Augmenting Bone Regeneration. *J. Control. Release* **2016**, *235*, 365–378. https://doi.org/10.1016/j.jconrel.2016.05.061.

(36) Okada, M.; Yano, K.; Namikawa, T.; Uemura, T.; Hoshino, M.; Kazuki, K.; Takaoka, K.; Nakamura, H. Bone Morphogenetic Protein-2 Retained in Synthetic Polymer/β-Tricalcium Phosphate Composite Promotes Hypertrophy of a Vascularized Long Bone Graft in Rabbits. *Plast. Reconstr. Surg.* **2011**, *127* (1), 98–106. https://doi.org/10.1097/PRS.0b013e3181f95a73.

(37) Schüller-Ravoo, S.; Feijen, J.; Grijpma, D. W. Preparation of Flexible and Elastic Poly(Trimethylene Carbonate) Structures by Stereolithography. *Macromol. Biosci.* **2011**, *11* (12), 1662–1671. https://doi.org/10.1002/mabi.201100203.

(38) Trachtenberg, J. E.; Placone, J. K.; Smith, B. T.; Fisher, J. P.; Mikos, A. G. Extrusion-Based 3D Printing of Poly(Propylene Fumarate) Scaffolds with Hydroxyapatite Gradients. *J. Biomater. Sci. Polym. Ed.* **2017**, *28* (6), 532–554. https://doi.org/10.1080/09205063.2017.1286184.

(39) Zeng, N.; van Leeuwen, A. C.; Grijpma, D. W.; Bos, R. R. M.; Kuijer, R. Poly(Trimethylene Carbonate)-Based Composite Materials for Reconstruction of Critical-Sized Cranial Bone Defects in Sheep. *J. Cranio-Maxillofacial Surg.* **2017**, *45* (2), 338–346.

https://doi.org/10.1016/j.jcms.2016.12.008.

(40) Fukushima, K. Poly(Trimethylene Carbonate)-Based Polymers Engineered for Biodegradable Functional Biomaterials. *Biomater. Sci.* **2016**, *4* (1), 9–24. https://doi.org/10.1039/C5BM00123D.

(41) Zhang, Z.; Kuijer, R.; Bulstra, S. K.; Grijpma, D. W.; Feijen, J. The in Vivo and in Vitro Degradation Behavior of Poly(Trimethylene Carbonate). *Biomaterials* **2006**, *27* (9), 1741–1748. https://doi.org/10.1016/j.biomaterials.2005.09.017.

(42) Bat, E.; Kothman, B. H. M.; Higuera, G. A.; van Blitterswijk, C. A.; Feijen, J.; Grijpma, D. W. Ultraviolet Light Crosslinking of Poly(Trimethylene Carbonate) for Elastomeric Tissue Engineering Scaffolds. *Biomaterials* **2010**, *31* (33), 8696–8705. https://doi.org/10.1016/J.BIOMATERIALS.2010.07.102.

(43) Rongen, J. J.; van Bochove, B.; Hannink, G.; Grijpma, D. W.; Buma, P. Degradation Behavior of, and Tissue Response to Photo-Crosslinked Poly(Trimethylene Carbonate) Networks. *J. Biomed. Mater. Res. Part A* **2016**, *104* (11), 2823–2832. https://doi.org/10.1002/jbm.a.35826.

(44) van Bochove, B.; Grijpma, D. W. Photo-Crosslinked Synthetic Biodegradable Polymer Networks for Biomedical Applications. *J. Biomater. Sci. Polym. Ed.* **2019**, *30* (2), 77–106. https://doi.org/10.1080/09205063.2018.1553105.

(45) Pêgo, A. P.; Grijpma, D. W.; Feijen, J. Enhanced Mechanical Properties of 1,3-Trimethylene Carbonate Polymers and Networks. *Polymer (Guildf).* **2003**, *44* (21), 6495–6504. https://doi.org/10.1016/S0032-3861(03)00668-2.

(46) Schüller-Ravoo, S.; Feijen, J.; Grijpma, D. W. Flexible, Elastic and Tear-Resistant Networks Prepared by Photo-Crosslinking Poly(Trimethylene Carbonate) Macromers. *Acta Biomater.* **2012**, *8* (10), 3576–3585. https://doi.org/10.1016/j.actbio.2012.06.004.

(47) Dienel, K. E. G.; van Bochove, B.; Seppälä, J. V. Additive Manufacturing of Bioactive Poly(Trimethylene Carbonate)/β-Tricalcium Phosphate Composites for Bone Regeneration.

Biomacromolecules **2020**, *21* (2), 366–375. https://doi.org/10.1021/acs.biomac.9b01272.

(48) van Bochove, B.; Hannink, G.; Buma, P.; Grijpma, D. W. Preparation of Designed Poly(Trimethylene Carbonate) Meniscus Implants by Stereolithography: Challenges in Stereolithography. *Macromol. Biosci.* **2016**, *16* (12), 1853–1863. https://doi.org/10.1002/mabi.201600290.

(49) Guillaume, O.; Geven, M. A.; Varjas, V.; Varga, P.; Gehweiler, D.; Stadelmann, V. A.; Smidt, T.; Zeiter, S.; Sprecher, C.; Bos, R. R. M.; Grijpma, D. W.; Alini, M.; Yuan, H.; Richards, G. R.; Tang, T.; Qin, L.; Yuxiao, L.; Jiang, P.; Eglin, D. Orbital Floor Repair Using Patient Specific Osteoinductive Implant Made by Stereolithography. *Biomaterials* **2020**, *233*, 119721. https://doi.org/10.1016/j.biomaterials.2019.119721.

(50) Guillaume, O.; Geven, M. A.; Sprecher, C. M.; Stadelmann, V. A.; Grijpma, D. W.; Tang, T. T.; Qin, L.; Lai, Y.; Alini, M.; de Bruijn, J. D.; Yuan, H.; Richards, R. G.; Eglin, D. Surface-Enrichment with Hydroxyapatite Nanoparticles in Stereolithography-Fabricated Composite Polymer Scaffolds Promotes Bone Repair. *Acta Biomater.* **2017**, *54*, 386–398. https://doi.org/10.1016/J.ACTBIO.2017.03.006.

(51) Teotia, A. K.; Raina, D. B.; Singh, C.; Sinha, N.; Isaksson, H.; Tägil, M.; Lidgren, L.; Kumar, A. Nano-Hydroxyapatite Bone Substitute Functionalized with Bone Active Molecules for Enhanced Cranial Bone Regeneration. *ACS Appl. Mater. Interfaces* **2017**, *9* (8), 6816–6828. https://doi.org/10.1021/acsami.6b14782.

(52) Melchels, F. P. W.; Bertoldi, K.; Gabbrielli, R.; Velders, A. H.; Feijen, J.; Grijpma, D. W. Mathematically Defined Tissue Engineering Scaffold Architectures Prepared by Stereolithography. *Biomaterials* **2010**, *31* (27), 6909–6916. https://doi.org/10.1016/j.biomaterials.2010.05.068.

(53) Lozinsky, V. I. Cryogels on the Basis of Natural and Synthetic Polymers: Preparation, Properties

and Application. *Russ. Chem. Rev.* **2002**, *71* (6), 489–511. https://doi.org/10.1070/RC2002v071n06ABEH000720.

(54) Kumar, A. *Supermacroporous Cryogels*; Kumar, A., Ed.; CRC Press, 2016. https://doi.org/10.1201/b19676.

(55) Lozinsky, V. I. Polymeric Cryogels as a New Family of Macroporous and Supermacroporous Materials for Biotechnological Purposes. *Russ. Chem. Bull.* **2008**, *57* (5), 1015–1032. https://doi.org/10.1007/s11172-008-0131-7.

(56) Lehtinen, P.; Kaivola, M.; Partanen, J. Absorption Cross-Sections of Disperse Orange 13 and Irgacure 784 Determined with Mask Projection Vat Photopolymerization. *Addit. Manuf.* **2018**, *22*, 286–289. https://doi.org/10.1016/j.addma.2018.05.006.

(57) Guillaume, O.; Geven, M. A.; Grijpma, D. W.; Tang, T. T.; Qin, L.; Lai, Y. X.; Yuan, H.; Richards, R. G.; Eglin, D. Poly(Trimethylene Carbonate) and Nano-Hydroxyapatite Porous Scaffolds Manufactured by Stereolithography. *Polym. Adv. Technol.* **2017**, *28* (10), 1219–1225. https://doi.org/10.1002/pat.3892.

(58) Ducheyne, P.; Radin, S.; King, L. The Effect of Calcium Phosphate Ceramic Composition and Structure Onin Vitro Behavior. I. Dissolution. *J. Biomed. Mater. Res.* **1993**, *27* (1), 25–34. https://doi.org/10.1002/jbm.820270105.

(59) Bartee, B. K.; Carr, J. A. Evaluation of a High-Density Polytetrafluoroethylene (n-PTFE) Membrane as a Barrier Material to Facilitate Guided Bone Regeneration in the Rat Mandible. *J. Oral Implantol.* **1995**, *21* (2), 88–95.

(60) Klein, C. P. A. T.; Driessen, A. A.; de Groot, K.; van den Hooff, A. Biodegradation Behavior of Various Calcium Phosphate Materials in Bone Tissue. *J. Biomed. Mater. Res.* **1983**, *17* (5), 769–784. https://doi.org/10.1002/jbm.820170505.

(61) Engler, A. J.; Sen, S.; Sweeney, H. L.; Discher, D. E. Matrix Elasticity Directs Stem Cell Lineage

Specification. *Cell* **2006**, *126* (4), 677–689. https://doi.org/10.1016/j.cell.2006.06.044.

For Table of Contents Only: